UNIVERSIDADE ESTADUAL DE CAMPINAS
Faculdade de Engenharia Mecânica

HENRIQUE BARBOSA DE OLIVEIRA

Micro fluidized beds: an experimental and numerical study on the effects of the inclination of a bidisperse bed

Micro leitos fluidizados: um estudo experimental e numérico sobre os efeitos da inclinação em leitos bidispersos

Campinas

2024

HENRIQUE BARBOSA DE OLIVEIRA

Micro fluidized beds: an experimental and numerical study on the effects of the inclination of a bidisperse bed

Micro leitos fluidizados: um estudo experimental e numérico sobre os efeitos da inclinação em leitos bidispersos

Thesis presented to the School of Mechanical Engineering of the University of Campinas in partial fulfillment of the requirements for the degree of Master in Mechanical Engineering, in the area of Thermal and Fluids.

Dissertação apresentada à Faculdade de Engenharia Mecânica da Universidade Estadual de Campinas como parte dos requisitos exigidos para a obtenção do título de Mestre em Engenharia Mecânica, na Área de Térmica e Fluidos .

Orientador: Prof. Dr. Erick de Moraes Franklin

ESTE TRABALHO CORRESPONDE À VERSÃO FINAL DA DISSERTAÇÃO DEFENDIDA PELO ALUNO HENRIQUE BARBOSA DE OLIVEIRA, E ORIENTADA PELO PROF. DR. ERICK DE MORAES FRANKLIN.

Campinas

2024

Ficha catalográfica
Universidade Estadual de Campinas (UNICAMP)
Biblioteca da Área de Engenharia e Arquitetura
Rose Meire da Silva - CRB 8/5974

OL4m

Oliveira, Henrique Barbosa de, 1999-
Micro fluidized beds : an experimental and numerical study on the effects of the inclination of a bidisperse bed / Henrique Barbosa de Oliveira. – Campinas, SP : [s.n.], 2024.

Orientador: Erick de Moraes Franklin.
Dissertação (mestrado) – Universidade Estadual de Campinas (UNICAMP), Faculdade de Engenharia Mecânica.

1. Leito fluidizado. 2. Fluidodinâmica computacional. 3. Processamento de imagens. 4. Materiais granulados. 5. Misturas. 6. Método dos elementos discretos. I. Franklin, Erick de Moraes, 1974-. II. Universidade Estadual de Campinas (UNICAMP). Faculdade de Engenharia Mecânica. III. Título.

Informações Complementares

Título em outro idioma: Micro leitos fluidizados : um estudo experimental e numérico sobre os efeitos da inclinação em leitos bidispersos
Palavras-chave em inglês:
Fluidized beds
Computational fluid dynamics
Image processing
Granular materials
Mixing
Discrete element method
Área de concentração: Térmica e Fluídos
Titulação: Mestre em Engenharia Mecânica
Banca examinadora:
Erick de Moraes Franklin [Orientador]
Cezar Otaviano Ribeiro Negrão
Rodolfo Marcilli Perissinotto
Data de defesa: 20-08-2024
Programa de Pós-Graduação: Engenharia Mecânica

Identificação e informações acadêmicas do(a) aluno(a)
- ORCID do autor: https://orcid.org/0000-0002-5138-5268
- Currículo Lattes do autor: https://lattes.cnpq.br/7030485088095658

UNIVERSIDADE ESTADUAL DE CAMPINAS
FACULDADE DE ENGENHARIA MECÂNICA

DISSERTAÇÃO DE MESTRADO ACADÊMICO

Micro fluidized beds: an experimental and numerical study on the effects of the inclination of a bidisperse bed

Micro leitos fluidizados: um estudo experimental e numérico sobre os efeitos da inclinação em leitos bidispersos

Autor: Henrique Barbosa de Oliveira

Orientador: Prof. Dr. Erick de Moraes Franklin

A Banca Examinadora composta pelos membros abaixo aprovou esta Dissertação:

Prof. Dr. Erick de Moraes Franklin, Presidente
Departamento de Energia/Faculdade de Engenharia Mecânica/Universidade Estadual de Campinas

Prof. Dr. Cezar Otaviano Ribeiro Negrão
Departamento Acadêmico de Mecânica/Universidade Técnológica Federal do Paraná

Dr. Rodolfo Marcilli Perissinotto
Centro de Estudos de Energia e Petróleo/Universidade Estadual de Campinas

A Ata de Defesa com as respectivas assinaturas dos membros encontra-se no SIGA/Sistema de Fluxo de Dissertação/Tese e na Secretaria do Programa da Unidade.

Campinas, 20 de agosto de 2024

DEDICATION

I would like to dedicate this work to my family that always supports me, in special to my parents Celso and Simone who taught me to pursue my dreams, also to my brothers Maurício and André who were always by my side.

I would also like to dedicate this thesis to my friends who joined me in this journey and made it much better.

ACKNOWLEDGEMENTS

This dissertation would not be possible without the aid from Prof. Dr. Erick de Moraes Franklin, who worked hard to help and guide me through this project.

To my laboratory colleagues, for their friendship, helpful conversations and all the support towards this work.

This study was financed in part by the São Paulo Research Foundation (FAPESP), grant 2022/08321-0.

No fim tudo dá certo, e se não deu

é porque não chegou ao final.

Fernando Sabino

RESUMO

Micro leitos fluidizados são basicamente suspensões de partículas sólidas por um escoamento ascendente em um tubo de escala milimétrica, com aplicações em processos industriais químicos e farmacêuticos envolvendo pós. Embora em muitas aplicações os leitos sejam polidispersos, trabalhos anteriores consideraram principalmente leitos monodispersos alinhados na direção vertical. Entretanto, introduzir uma inclinação com relação à gravidade leva a diferentes padrões no leito e níveis de mistura, o que pode ser benéfico para algumas aplicações. Nesta dissertação, investiga-se o comportamento de micro leitos fluidizados por gás utilizando misturas bidispersas sob diferentes inclinações. Nos experimentos, leitos mono- e bidispersos são filmados com uma câmera rápida, e as imagens são processadas para obter medidas na escala do leito e dos grãos. Observa-se segregação mais pronunciada em leitos verticais, e ainda que a mistura de partículas varia não monotonicamente com a inclinação, com um máximo de mistura entre os ângulos de 30° a 45° com relação à gravidade. A camada de mistura se forma pela competição entre a separação cinética e a circulação local promovida pelo escoamento, o que é revelado calculando a média e flutuações das velocidades das partículas. Pior fluidização também é observada conforme o ângulo com a vertical aumenta, o que explica o comportamento não monotônico. Simulações numéricas são desenvolvidas com a técnica CFD-DEM para replicar os resultados experimentais, de modo a revelar mais informações sobre o escoamento. Esses resultados apresentam novas perspectivas sobre mistura e segregação em leitos polidispersos, o que pode ser explorado para processamento de pós em aplicações industriais. Parte dessa dissertação foi redigida com base em Oliveira e Franklin (2024).

Palavras–chave: Leito fluidizado. Ângulo. Processamento de imagens. Materiais granulados. Mistura. Segregação. Fluidodinâmica computacional. Método de elementos discretos.

ABSTRACT

Micro fluidized beds are basically suspensions of solid particles by an upward fluid flow in a millimeter-scale tube, with applications in chemical and pharmaceutical processes involving powders. Although in many applications beds are polydisperse, previous works considered mostly monodisperse beds aligned in the vertical direction. However, introducing an inclination with respect to gravity leads to different bed patterns and mixing levels, which can be beneficial for some applications. In this MSc Thesis, the behavior of micro gas-solid beds using bidisperse mixtures under different inclinations is investigated. In the experiments, mono- and bidisperse beds are filmed with a high-speed camera, and the images are processed to obtain measurements at bed and grain scales. It is seen that the degree of segregation is larger for vertical beds, and also that mixing varies non-monotonically with inclination, with a maximum degree of mixing in angles between 30°-45° with respect to gravity. The mixing layer forms by the competition between kinetic sieving and local circulation promoted by the fluid flow, which is revealed by computing the mean and the fluctuations of the particles' velocities. Worse fluidization is also observed as the angle relative to the vertical increases, accounting then for the non-monotonic behavior. Numerical simulations are developed within the CFD-DEM framework to mimic the experiments, in this way more information about the fluid flow is revealed. These results bring new insights into mixing and segregation in polydisperse beds, which can be explored for processing powders in industry. Part of this MSc Thesis was written based on Oliveira and Franklin (2024).

Keywords: Fluidized beds. Inclination. Image processing. Granular materials. Mixing. Segregation. Computational fluid dynamics. Discrete element method.

LIST OF FIGURES

LIST OF TABLES

LIST OF ACRONYMS

CFD-DEM	Computational Fluid Dynamics - Discrete Element Method
CMOS	Complementary Metal-Oxide-Semiconductor
FCC	Fluid Catalytic Cracking
ID	Inner Diameter
LAMMPS	Large-scale Atomic/Molecular Massively Parallel Simulator
LED	Light Emitting Diode
LIGGGHTS	LAMMPS Improved for General Granular and Granular Heat Transfer Simulations
MFB	Micro Fluidized Beds
NFB	Narrow Fluidized Bed
OpenFOAM	Open source Field Operation And Manipulation
OVITO	Open Visualization Tool
PISO	Pressure Implicit with Splitting of Operators
ROI	Region Of Interest

LIST OF SYMBOLS

Latin letters

A_f	flux of particles measured by area	$[m/s]$
Ar	Archimedes number, $Ar = gd_p^3(\rho_p - \rho_f)\rho_f/\mu_f^2$	$[-]$
C	celerity of plugs propagating in the fluidized bed	$[m/s]$
CT	concentration of tracer particles	$[-]$
C_d	drag coefficient	$[-]$
D	tube inner diameter	$[mm]$
Dn	discriminative number	$[-]$
d	spheres diameter	$[mm]$
e	restitution coefficient	$[-]$
E	layer separation	$[-]$
$F_{p,f}$	drag force per volume	$[N/m^3]$
F_c	contact force	$[N]$
G^*	average shear modulus, $\frac{1}{G^*} = \frac{2(2-\nu_1)(1+\nu_1)}{Y_1} + \frac{2(2-\nu_2)(1+\nu_2)}{Y_2}$	$[Pa]$
g	gravity acceleration	$[m/s^2]$
h	fluidized bed height	$[mm]$
I	moment of inertia	$[kg\ m^2]$
k	elastic constant	$[N/m]$
L	bed moment	$[m^2/s]$
l	particle traveled distance	$[m]$
M	mixing index	$[-]$
m	total mass of grains	$[kg]$
m_p	particle mass	$[kg]$
N	number of particles	$[-]$
P	pressure	$[Pa]$
Q	volumetric flow rate	$[m^3/s]$
R^*	average radius, $\frac{1}{R^*} = \frac{1}{R_1} + \frac{1}{R_2}$	$[m]$
R_{sl}	drag force exchanged between fluid and particles	$[N]$

Re_D	Reynolds number based on the tube diameter	$[-]$
Re_d	Reynolds number based on the particle diameter	$[-]$
Re_{mf}	Reynolds number based on the tube diameter and minimum fluidization velocity	$[-]$
Re_t	Reynolds number based on the particle diameter and terminal velocity	$[-]$
S	standard deviation	$[-]$
S_n	normal rigidity, $S_n = 2Y^* \sqrt{R^* \delta_n}$	$[kg/s^2]$
S_t	transversal rigidity, $S_t = 8G^* \sqrt{R^* \delta_t}$	$[kg/s^2]$
St_t	Stokes number based on the terminal velocity of a single particle	$[-]$
T_p	torque applied on the particle	$[Nm]$
t	time	$[s]$
U	velocity	$[m/s]$
U_{p0}	terminal velocity of a settling particle	$[m/s]$
u	velocity component aligned with the x-axis	$[m/s]$
V_{cell}	volume of calculation cell	$[m^3]$
V_p	volume of the particle	$[m^3]$
v	velocity component aligned with the y-axis	$[m/s]$
w	velocity component aligned with the z-axis	$[m/s]$
x_μ	static friction coefficient	$[-]$
Y	Young modulus	$[Pa]$
Y^*	average Young modulus, $\frac{1}{Y^*} = \frac{1-\nu_1^2}{Y_1} + \frac{1-\nu_2^2}{Y_2}$	$[Pa]$
z	vertical position in the bed	$[mm]$

Greek letters

α	volumetric fraction of fluid (void fraction)	$[-]$
β	moment exchange coefficient (Gidaspow)	$[-]$
γ	viscous dissipation	$[N\ s/m]$
Δx	cell width on the CFD numerical mesh	$[m]$
δ	particle superposition	$[m]$
θ	granular temperature	$[m^2/s^2]$
λ	plug length	$[mm]$
μ	dynamic viscosity	$[Pa\ s]$
ν	Poisson coefficient	$[-]$
ρ	density	$[kg/m^3]$
τ	newtonian stress tensor	$[Pa]$
φ	bed inclination	$[deg]$
ϕ	volumetric fraction of solids (packing fraction)	$[-]$
ψ	$\psi = ln(e)/\sqrt{ln^2(e) + \pi^2}$	$[-]$
ω	rotation speed	$[rad/s]$

Subscripts

a	air
e	flow entry surface
f	fluid
ff	fixed bed
g	glass particles
if	incipient fluidization
inv	inversion
mf	minimum fluidization
n	normal component
p	particles
t	tangent component
w	wall
z	zirconium particles

CONTENTS

1 INTRODUCTION

Fluidization is the suspension of particles by a fluid (gas or liquid) in upward flow, in which the grains' weight is in balance with the drag. This phenomenon is characterized by the solids behaving similar to a liquid up to a certain point, which improves heat and mass exchange rates, disseminating the use of fluidized beds in many different processes (Kunii; Levenspiel, 1991).

The first use of fluidized beds as industrial equipments with commercial success was in the coal gasification to burn in boilers. It was atfer popularized with other processes such as the Fluid Catalytic Cracking (FCC) (Kunii; Levenspiel, 1991). These uses, in general, happen in large dimension beds, though recently there are new developments which require smaller equipments.

The study of Micro Fluidized Beds (MFB) have advanced in the last few years specially for the applications not suited to regular beds. Such as the use in the research of burning efficiency of solid biofuels, with better control over the combustion parameters (Guo *et al.*, 2009), coating of solids (Schreiber *et al.*, 2002; Rodríguez-Rojo *et al.*, 2008), carbon capture with greater efficency (Fang *et al.*, 2009; Shen *et al.*, 2019), bioproduction (Wu *et al.*, 2007; Pereiro *et al.*, 2017; Liu *et al.*, 2010), gasification (Fig. 1.1) (Zhang *et al.*, 2015; Cortazar *et al.*, 2020; Zeng *et al.*, 2014), pyrolisis (Yu *et al.*, 2011; Mao *et al.*, 2015; Gao *et al.*, 2017; Jia *et al.*, 2017), catalytic cracking (Guo *et al.*, 2016; Boffito *et al.*, 2014), micro chemical reactors (Suryawanshi *et al.*, 2018) and especially in pharmaceutical industries to produce pills and tablets (Shi *et al.*, 2019; Azad *et al.*, 2018; Katstra *et al.*, 2000; Fung; Ng, 2003) and powder vaccines (Huang *et al.*, 2004; Gomez *et al.*, 2021).

There are advantages directly from the size reduction, for example the reduced cost of building and operating the fluidized bed, less energy consumption and improved control over the reactions analyzed (Zhang *et al.*, 2021). Though the smaller size can lead to a higher confinement of particles, in this case the size of particles is close to the tube inner diameter and these are called narrow beds. This can present unusual behaviors compared to regular beds, like the propagation of instabilities through the tube, consisting of alternating regions of high (plugs) and low (bubbles) solid concentration (Cúñez; Franklin, 2019), and crystallization and jamming (Cúñez; Franklin, 2020a; Oliveira *et al.*, 2023). Crystallization is the formation of a

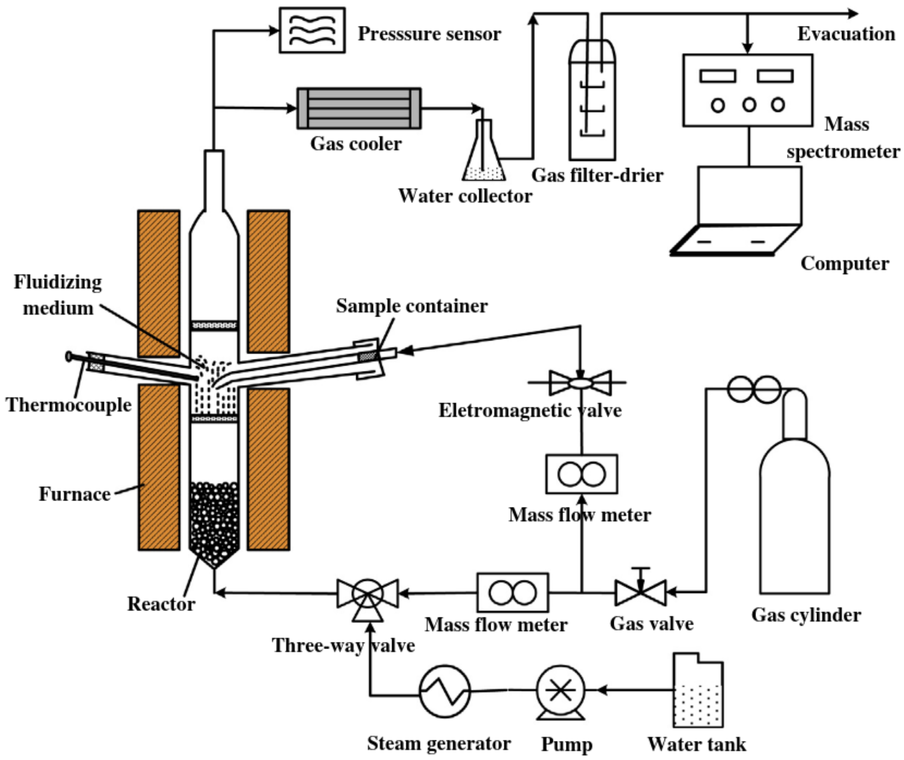

Figure 1.1 – Example of a micro fluidized bed reactor, reproduced from Zhang *et al.* (2015).

regular structure of particles in the bottom of the bed, that do not present large scale motion. On the other hand, jamming refers to the formation of a block of particles, in which even the small scale agitation of the grains is suppressed. Which should be studied to improve the applications of MFBs (Guo *et al.*, 2009) in different areas.

In real applications fluidized beds are usually polydisperse, with different types of grains varying in size, density and shape. Bidisperse fluidized beds are a simplification of this case with two types of particles, which can be used to start the investigation of the effects of polydispersity in fluidization. With this simpler case it is already possible to observe new behaviors, such as the appearance of stable layers containing only each type of particle, with little particle mixing, and layer inversion depending on the initial condition (Cúñez; Franklin, 2020b).

For some applications the concentration profile of the different types of solids is important, like biomass combustion (Wu *et al.*, 2019), therefore strategies to promote mixing were developed. It is possible to promote particle mixing by inclining the fluidized bed with respect to the gravity direction, as described by Chaikittisilp *et al.* (2006). Hudson *et al.* (1996) observed a circulation pattern in inclined beds and proposed a hypothesis that it prevents the formation of particle layers. Other consequences of tilting the gas-solid bed are the appearance of an air channel above the solids (O'Dea *et al.*, 1990) and a decrease in the bed expansion (Yi *et al.*, 2022).

To better understand the dynamic of fluidized beds, in special those with reduced number of particles, in the last few years there was an increase in the use of computational simulations of the type Computational Fluid Dynamics - Discrete Element Method (CFD-DEM) to analyze this kind of problem, due to the higher accessibility of computational power to researchers (El-Emam *et al.*, 2021). Cúñez and Franklin (2019) used this approach to analyze the formation of plugs in a liquid-solid narrow fluidized bed and found that the force chains extended through the entire cross-section of the tube. This shows some of the advantages of numerical simulations to investigate contact forces and the particles inside the bed that are not visible from the outside in experimental studies, for example.

This study aims to understand how inclining a bidisperse gas-solid micro fluidized bed affects the fluidization characteristics and the mixing of particles. By using experiments and numerical simulations, the dynamics of fluidization can be better understood, as well as improve the knowledge about how the particles' individual motion affect the general behavior of the bed. This can also advance applications of micro fluidized beds which benefit from a mixing of different particle types. The numerical simulations are used to extend the experiments, by reproducing the observed results it is possible to extend further the exploration of micro fluidized beds accessing quantities that cannot be observed filming the side of the bed. It is possible to track every particle individually, analyzing its motion and interactions with the other particles, the walls and the fluid.

1.1 Objectives

1.1.1 General objectives

- Explore the effect of inclining a bidisperse micro fluidized bed in the mixing of particles with experiments and numerical simulations to get insights into the dynamics of fluidization in these conditions.

1.1.2 Specific objectives

- Explore the effects of inclination in a bidisperse micro fluidized bed, analyzing the mixing of glass and zirconium particles fluidized by air.

- Reproduce the experiments using numerical simulations and compare both results.
- Use the numerical simulations to gain insights in the behavior of individual particles inside the beds and the fluid-particle interactions.

1.2 Publications related to the dissertation

The results described in this dissertation are also present in the following journal papers and conference proceedings:

- Oliveira, H. B. & Franklin, E. M. *Bidisperse micro fluidized beds: Effect of bed inclination on mixing*. Physics of Fluids, 36, 013303 (2024).
- Oliveira, H. B. & Franklin, E. M. *Particle segregation in bidisperse narrow beds fluidized at different inclinations*. In: 27th International Congress of Mechanical Engineering - COBEM2023, Florianópolis, Brazil, 2023.

2 LITERATURE REVIEW

This chapter concerns about fundamental concepts of fluidized beds and explore the literature developments about narrow and micro fluidized beds, which are variations of regular beds that can be used in some applications. They also present different types of instabilities and behaviors that were explored over the years. The known effects of inclining the tube on fluidization are also presented as consequences of modifying how gravity affect the ensemble of particles and bed instabilities. Other aspect to be reviewed is the mixing and segregation effects on bidisperse beds, where two types of particles are present. Recently, numerical simulations were used to model this phenomenon, the main tools and models to do that are also explained in this section, highlighting the importance of this new technique to understand better some aspects of fluidization.

2.1 Fluidization

Fluidization is a phenomenon in which solid particles are suspended by an ascending fluid flow, gas or liquid, what promotes the agitation and movement of the particles that can resemble a fluid, hence the denomination of fluidized beds for processes that explore this technique. There are several applications that benefit from improved heat and mass transfer between particles and fluid. Bello *et al.* (2017) reviewed the applications of fluidized bed reactors in the wastewater treatment using oxidation, biological and adsorption processes due to the good contact between water and solids. They assessed that these technics have the potential to improve performance and contribute to cleaner production in industries. Capece and Dave (2011) studied the coating of membranes onto catalysts using fluidized beds and reported good uniformity and controllability of the process, which highlights the possibility of using fluidization to achieve proper coating of particles, both in food (Dewettinck; Huyghebaert, 1999) and pharmaceutical industries (Silva *et al.*, 2014). Throughout the development of fluidized beds some uses gained commercial popularity, such as Fluid Catalytic Cracking (Chen, 2003), gasification and combustion of carbon fuels, such as biomass and coal (Newby, 2003) and chemical reactors (Jazayeri, 2003). The many industrial applications motivated investigations and many studies in these topics to better understand the process, improving efficiency and applicability.

To study this subject some appropriate nomenclatures were developed, therefore a few relevant terms are presented next. The average velocity of the fluid entering the bed is denominated the superficial velocity, usually calculated by the division of the volumetric flow rate by the cross-sectional area of the tube. When subjected to fluid flow at a critical velocity (U_{mf}), a fluidized bed usually shows a liquid-like movement of the particles and presents a pressure drop equal to the bed weight (solids and fluid), this state is denominated minimum fluidization (Kunii; Levenspiel, 1991). When pressure measurement is not possible, the minimum fluidization condition can be estimated by the incipient fluidization velocity (U_{if}), which is the lowest superficial velocity that causes particles' movement to be observed.

Different patterns of behavior can be observed dependent on the physical properties of particles and superficial velocity (Kunii; Levenspiel, 1991). The main characteristics of each classification are enumerated next:

- Fixed bed: At low superficial velocities the fluid flows around the particles without affecting them, in a condition in which fluidization is not observed.
- Uniform fluidization: the particles are evenly distributed across the bed with a uniform packing fraction.
- Bubbling fluidization: bubbles of fluid are present within the particle phase.
- Slugging fluidization: similar to the bubbling regime, but the fluid pockets are larger and extend through the entire cross-section of the tube.
- Turbulent fluidization: it occurs at high superficial velocities when entrainment of solids becomes more relevant and instead of bubbles, complex solids and fluid structures move in a turbulent motion.
- Lean phase fluidization: it is observed with high enough fluid velocity and the solids are transported pneumatically.

A typical classification of particles is based on their behavior when fluidized by a gas observed by Geldart (1973), where type A particles expand uniformly after minimum fluidization before bubbling can be observed. Type B bubble just at minimum fluidization and uniform fluidization cannot be achieved, type C particles are difficult to fluidize and, finally, type D form spouted beds easily. Despite the classification being based on the fluidization behavior, the types can be predicted by the mean size of particles and difference of density between particles and gas ($\rho_p - \rho_a$) as seen in Figure 2.1.

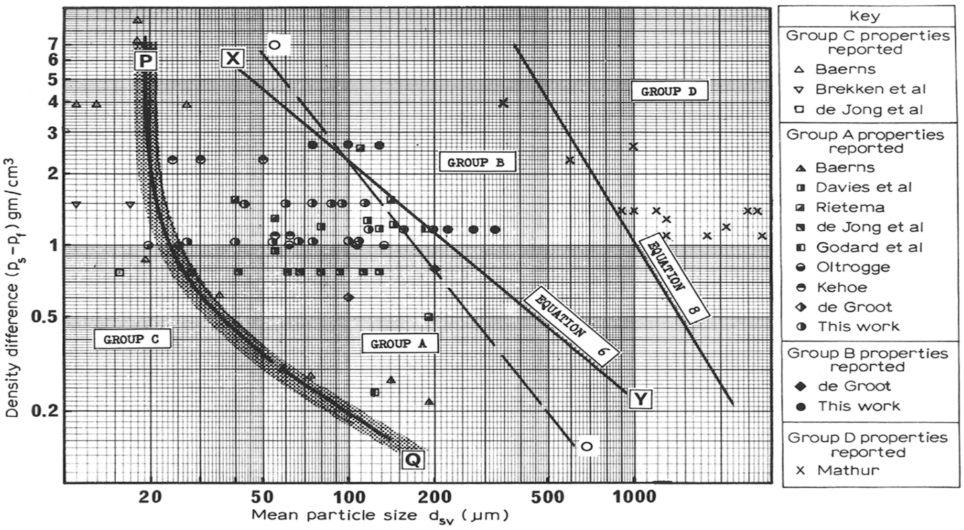

Figure 2.1 – Diagram with the Geldart classification, the solid density is defined as ρ_s by the author and represents the particle density ρ_p in this thesis. Reproduced from Geldart (1973).

Another important parameter to characterize fluidization is the volumetric fraction of particles (ϕ), which represents how much of the volume of a given region is occupied by particles (also called packing fraction). And also its compliment ($\alpha = 1 - \phi$) is denominated de voidage of the bed (or void fraction) and measures the fluid volume compared to the region volume. This quantity is sensitive to the volume used for calculation, as large volumes can average across small variations of particle concentration, but small volumes approaching the particle size are affected by local variations and individual particle movement. Richardson and Zaki (1954) found an experimental correlation between fluid velocity (U_f), solid volumetric fraction (ϕ) and the terminal velocity of a settling particle (U_{p0}) for beds that expand uniformly given in Equation 2.1.

$$U_f = U_{p0} \left(1 - \phi\right)^n \tag{2.1}$$

The exponent n is adjusted with experimental data for 4 ranges by the authors, like $n = 4.45 Re_d^{-0.1}$ for $200 < Re_d < 500$. Later, Rowe (1987) adjusted an empirical model (Eq. 2.2) for the exponent, in which Re_t is the Reynolds number of a single particle based on the terminal velocity. Other adaptations were made to accommodate different types of particles, for example the work of Valverde *et al.* (2008) with magnetic particles type B by Geldart classification.

$$n = 2.35\frac{2 + 0.175Re_t^{3/4}}{1 + 0.175Re_t^{3/4}} \tag{2.2}$$

Many aspects of fluidized beds are connected to instabilities propagating through the tube, like the presence of bubbles and slugging fluidization. Jackson (1963) showed that uniform beds, with constant voidage (α) in every location, are unstable to voidage fluctuations as long as the drag acting on the particles increases with packing fraction (ϕ), which is often the case with the current drag models. There is also an exploration of the effect of the Froude number (Eq. 2.3), which indicates that higher Fr implies faster growth of instabilities. Anderson and Jackson (1968) also showed that beds in the state of uniform fluidization are unstable to small perturbations in particle volume fraction. By using an improved model that presents the most unstable mode with a finite wavelength, unlike the previous model that were most unstable to a zero wave number. Moreover, they described that the instabilities growth rate is larger in beds fluidized by gas compared to liquids, which is similar to what is observed in the Geldart classification (Geldart, 1973).

$$Fr = \frac{U_{mf}^2}{gd_p} \tag{2.3}$$

The Froude number is usually a ratio between fluid inercia and the strength of an external field (gravity). In the case of fluidized beds, it can be used to predict the behavior of the particles, with $Fr \ll 1$ it is expected an aggregative behavior and a bubbling bed, and $Fr \gg 1$ leads to particulate behavior and an uniform fluidization. Glasser *et al.* (1997) suggested that the division of uniform and bubbling beds might be close to a Froude number between 16 and 20. Another dimensionless number that can be used to characterize fluidized beds is the discriminative number proposed by Liu *et al.* (1996) as described in Equation 2.4.

$$Dn = \left(\frac{Ar}{Re_{mf}}\right)\left(\frac{\rho_p - \rho_f}{\rho_f}\right) \tag{2.4}$$

In which the Archimedes number (Ar) can be calculated by the Wen and Yu equation $Ar/Re_{mf} = 1650 + 24.5Re_{mf}$ (Wen; Yu, 1966), ρ_p and ρ_f are the density of the particles and fluid respectively. The work of Liu *et al.* (1996) suggested that the bed is particulated (homogenous fluidization) for $Dn \leq 10^4$, transitional for $10^4 \leq Dn \leq 10^6$ and aggregative (bubbling or slugging) for $Dn \geq 10^6$. The different bed behaviors are described in the diagram in Figure 2.2, with the particulated regime in the bottom and aggregative regimes in the top.

Beyond particle and fluid properties, the relationship between particle and tube sizes is also important as explained in the following section.

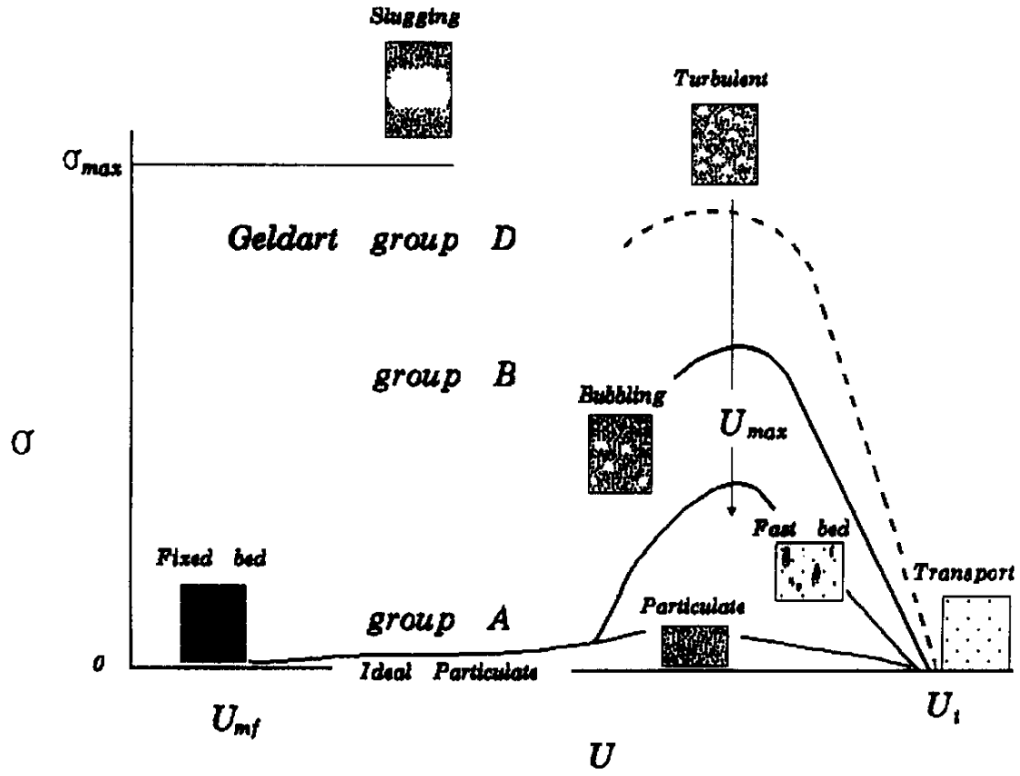

Figure 2.2 – An idealized profile of standard deviation of bed voidage α across the bed as function of average fluid velocity $\bar{U}$, reproduced from Liu *et al.* (1996).

2.1.1 Narrow fluidized beds

A specific type of bed is the Narrow Fluidized Bed (NFB), defined by the similar diameter of the bed tube and the particles ($D/d \approx 10$) (Cúñez; Franklin, 2020a) and the very-narrow fluidized beds with even lower diameter ratio, which is explored in this work. The literature dedicated to narrow fluidized beds shows that a higher confinement of the particles induces effects not present in regular fluidized beds, such as the formation of granular plugs and bubbles with low solid density extending for the entire bed cross-section (slugging regime). These phenomena are interesting because they differ from the expected behavior of a regular gas fluidized bed, which presents a bubbling regime with gas inlet velocities slightly above minimum fluidization (Du *et al.*, 2005; Homsy *et al.*, 1980), as it is hard to achieve uniform fluidization in a gas-solid bed.

The large particles compared to the bed can present problems to fluidize properly, Cúñez and Franklin (2020a) showed the formation of granular arches that stop the particle movement (jamming) in liquid-solid narrow fluidized bed. Furthermore, they described the formation of crystal-like structures that formed from the bottom of the bed and grew towards the top. Which prevented the large-scale motion of the particles, but the small fluctuations are still present unlike in jamming conditions, which is referred as crystallization (Fig. 2.3). Later, Oliveira *et al.* (2023) showed that crystallization can break down, the bed refluidizes and the cycle can repeat during the experiments.

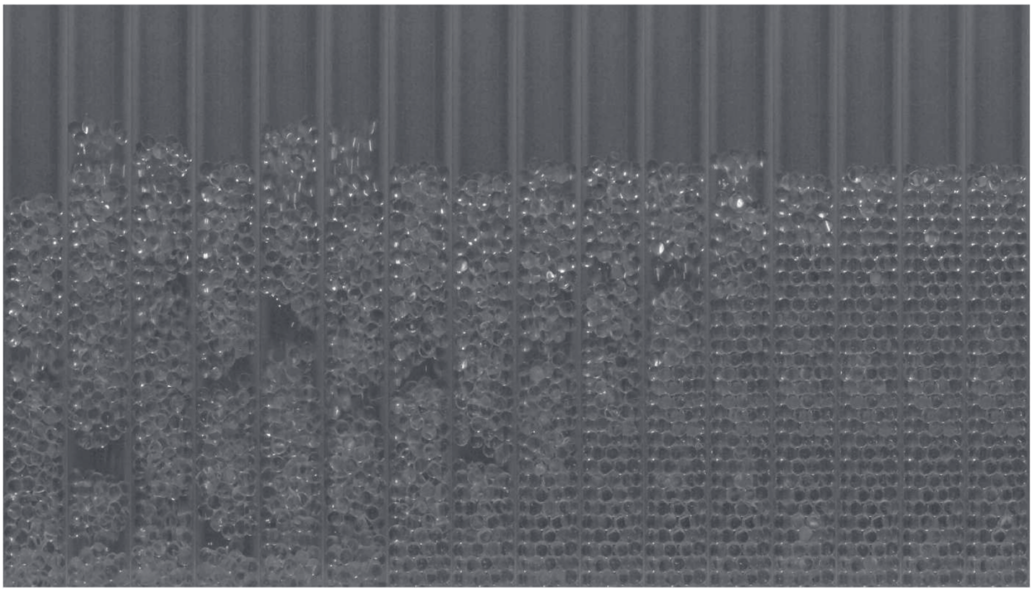

Figure 2.3 – Snapshots placed side by side of a narrow fluidized bed undergoing crystallization, reproduced from Cúñez and Franklin (2020a). The time between consecutive frames is $5\,\mathrm{s}$.

The plugs were studied by Cúñez and Franklin (2019) experimentally to measure the characteristic length and celerity when propagating through the bed. Numerical simulations were also conducted and the plugs characteristics compared, with a good agreement in the celerity with error in the order of 10%. Force chains were examined in the simulations and demonstrated the importance of arches extending through the cross-section of the plug. Later, Cúñez *et al.* (2021) analyzed the motion of bonded particles fluidized by water in narrow beds numerically and experimentally, they observed a reduction in plug length with increased water superficial velocity as with loose spheres. Also, that bonded particles are confined to specific regions in the bed, different from single spheres that traverse the entire bed.

Narrow beds can be formed in any size of tube, as the definition concerns the ratio of particles and tube diameters. But one common occurrence is in beds of reduced size that approaches the particles' diameter, this reduced size beds are subject of active research as explored in the next section.

2.1.2 Micro fluidized beds

Even though there is no consensus in the definition of a micro fluidized bed based on the inner diameter of the bed, it is usually defined as a tube diameter in the mm- or cm-scale (Zhang *et al.*, 2021; Qie *et al.*, 2022). This kind of bed is currently used in integrated DNA analyses (Hernández-Neuta *et al.*, 2018), carbon capture (Raganati *et al.*, 2014a; Raganati *et al.*, 2014b) and solid's coating (Schreiber *et al.*, 2002; Rodríguez-Rojo *et al.*, 2008). There is also an interest from chemical and pharmaceutical industries for powder processing, such as particle encapsulation (Schreiber *et al.*, 2002; Rodríguez-Rojo *et al.*, 2008), production of tablets and pills (Shi *et al.*, 2019; Azad *et al.*, 2018; Azad *et al.*, 2019; Katstra *et al.*, 2000; Kornblum; Hirschorn, 1970; Fung; Ng, 2003; Ervasti *et al.*, 2015), development of vaccines in powder form (Heida *et al.*, 2022; Amorij *et al.*, 2008; Jiang *et al.*, 2006; Gomez *et al.*, 2021; Huang *et al.*, 2004), gasification (Zeng *et al.*, 2014; Zhang *et al.*, 2015; Cortazar *et al.*, 2020), wastewater treatment (Kwak *et al.*, 2020; Kuyukina *et al.*, 2009) and bioproduction (Pereiro *et al.*, 2017; Wu *et al.*, 2007).

This large interest in MFBs has motivated works to understand how the smaller size affects fluidization. Many applications have the solids with diameters close to the tube size and are also narrow fluidized beds with similar conclusions to the previous section. Nevertheless, a few changes are observed compared to larger size beds due to adhesion forces becoming more relevant. Experimental results obtained with micro gas fluidized beds show an increase in the minimum fluidization velocity with the reduction of the inner diameter of the tube in which the experiments are performed. This represents a significant difference to the consolidated theory to larger fluidized beds, with inner diameter above $5\ \mathrm{mm}$ (Guo *et al.*, 2009). Also, it is verified that the pressure drop through the bed of small diameter is less than predicted using the correlations obtained to larger beds, due to the more pronounced effects of the solids-wall contact (Guo *et al.*, 2009; Cúñez; Franklin, 2019). There is the formation of arcs of particles from wall to wall that hold part of the bed weight and reduces the fraction supported by the fluid pressure drop.

Cúñez and Franklin (2023) analyzed experimentally a gas-solid MFB and found that instabilities propagate in the bed, formed by plugs and bubbles alternating in the column. The average height of the bed increases with a higher superficial velocity and higher flow velocity also decrease the plug length, increases plug celerity (which is the velocity with which the plug travels along the tube) and promotes plug-plug collisions. They also found that the particle agitation is lower inside plugs compared to bubbles and higher flow velocity promotes particle agitation due to smaller plugs, higher celerity and more plug-plug collisions.

This kind of insights help to improve the applications of micro fluidized beds in the industry and to understand more about the mechanisms that explain the observed characteristics of the bed, such as the instabilities and bed expansion. In this section most works focused on beds formed by a single particle type, but the presence of different particles may affect the fluidization as explored in the following section.

2.1.3 Bidisperse fluidized beds

Fluidized beds in industrial applications are typically polydisperse, meaning that multiple types of particles are present, with different densities, sizes or shapes. To study how this affects fluidization a simplification can be made in some cases, using just two types of particles, which is called a bidisperse bed.

Many experiments show segregation of different types of particles in bidisperse beds. A nomenclature was developed to identify the particle types by the segregating behavior, the particles with tendency to accumulate in the surface are called flotsam and the particle type that concentrates in the bottom of the bed is referred as jetsam. Renzo *et al.* (2020) investigated experimentally the layer inversion problem in binary mixtures, when smaller denser particles and larger less dense particles are fluidized. They reported that the Particle Segregation Model, derived from an analysis of forces acting on the solids, predicted accurately the inversion voidage of the experiments. Which is the average volumetric fraction when the segregation changes from density prevailing to size prevailing.

In other cases with higher superficial velocity mixing can be observed in the bed. Gibilaro and Rowe (1974) described a model for the solid concentration profile in the axial direction. This model was developed to represent bubbling beds, with a bulk phase with higher particle volume and the wake phase with higher fluid concentration that represents the bubbles rising in the bed. To represent this complex phenomenon it accounts for circulation of solids in the bed, exchange of particles between bulk and wake phases, axial mixing caused by the passage of bubbles and the tendency of solids to segregate by kinetic sieving.

2.1.4 Inclined fluidized beds

A deviation from the vertical direction affects significantly the fluidization because gravity no longer aligns with the axial direction of the fluidized bed. Hudson *et al.* (1996)

observed experimentally the circulation of solids by analyzing the vertical flux of solids in a cm-scale liquid-solid fluidized bed inclined up to 10°. They also observed an increase in minimum fluidization velocity (U_{mf}) when compared to vertical beds, furthermore they observed that the segregation of lighter tracer particles can be avoided with inclination and pointed to the circulation as a mechanism that prevents segregation of particles. O'Dea *et al.* (1990) characterized a channeling regime in which an air channel forms above a fixed the bed, and this happens at a specific fluid velocity that marks the stabilization of the pressure drop in the bed despite increasing the superficial velocity (similar to the minimum fluidization condition). The study was conducted experimentally with inclinations up to 45° in cm-scale gas-solid fluidized beds. They also found that the Ergun equation for pressure drop in a fixed bed is still valid in inclined beds.

Pozo *et al.* (1992) investigated inclined three-phase fluidized beds, this means that a gas-liquid-solid bed is used, with small inclinations up to 1.5° to explore the effects of not controlling adequately if the bed is tilted. They found that the bed height decreases with inclination and liquid-solid mass and heat transfer improves with a slight inclination, but the gas-liquid mass transfer coefficient can increase or decrease and is very sensitive to tilting.

These effects may be investigated in physical experiments and also in numerical simulations. Chaikittisilp *et al.* (2006) performed CFD-DEM simulations with gas-solid fluidized beds inclined up to 30° and reported good agreement with literature experiments. They also showed circulation of solids inside the bed and an increase of the fraction of the particles in a fixed bed with more inclined beds, as an air channel forms in the upper part of the tube. Li *et al.* (2017b) also performed CFD-DEM simulations but in a gas-solid micro fluidized bed inclined up to 45°, they reported the formation of an air channel as well and that the pressure drop decreases with inclination for the same bed condition and superficial velocity. These results show the importance of studying and developing numerical models capable of representing fluidization.

2.2 Numerical modeling

Studies focused on the computational modeling of fluidized beds were conducted utilizing the methodology CFD-DEM and present a good agreement with the experimental results in aspects such as: (i) characteristics of the bed expansion (Li *et al.*, 2021); (ii) velocity of minimum fluidization (U_{mf}); (iii) average pressure drop and frequency of oscillation; (iv) size and velocity of bubbles in the bubbling regime (Liu; van Wachem, 2019). Feng and Yu (2004) compared different models to calculate the force exchange between particles and fluid, the comparison with experiments revealed that models based on drag force correlations were more accurate in the gas-solid beds used in the study. Later, Feng and Yu (2007) applied numerical simulations to bidisperse beds with different sized particles, they found that there is an optimal fluid velocity for the segregation of solids by size, below that velocity the bed is in a fixed condition and above the higher agitation promotes mixing. The forces acting on the particles were measured and used to explain the segregation mechanism, which demonstrate the great advantage of numerical simulation in being able to access information about individual particles that would be difficult to acquire experimentally.

The Euler-Lagrange approach divides the problem in two parts, the fluid's behavior is calculated using a CFD model which better represents the expected flow, and the particles' behavior is calculated with a DEM model. Both approaches are integrated using the effects that each phase causes in the other. Therefore, it is important to choose correctly the drag model used, because it is a parameter changed in many studies to better represent each type of fluidized bed, in special when the bed is outside the size range used to derive the models (Liu; van Wachem, 2019).

The numerical simulations of fluidized beds may be performed at open source software, as presented in the next section, which allows a greater number of people to explore this subject and contribute to a better understanding of micro fluidized beds.

2.2.1 CFDEM®coupling

The open source software CFDEM®coupling (Goniva *et al.*, 2012) may be used to simulate a fluid flow, in an Eulerian frame of reference, coupled with the simulation of a group of particles, in a Lagrangian frame of reference. The CFD part is handled by the software OpenFOAM (Open source Field Operation And Manipulation) and the calculations involving solids are handled by the software LIGGGHTS (LAMMPS Improved for General Granular and Granular Heat Transfer Simulations) (Kloss *et al.*, 2012), which is based on the atomic simulation software LAMMPS (Large-scale Atomic/Molecular Massively Parallel Simulator).

The software is designed to be as general as possible, therefore there are multiple models to be chosen when defining the simulation parameters, as explained in the following section about the interaction between fluid cells and the particles.

2.2.2 Computational Fluid Dynamics

To handle the CFD numerical model, the OpenFOAM software was used in this thesis with the "pisoFoam" solver. Which solves the Navier-Stokes equations (Eq. 2.6) with the Pressure Implicit with Splitting of Operators (PISO) algorithm in mesh grid that divides the simulation domain.

$$\frac{\partial \alpha}{\partial t} + \nabla \cdot \left(\alpha \vec{U}\right) = 0 \tag{2.5}$$

$$\frac{\partial \left(\alpha \vec{U}\right)}{\partial t} + \nabla \cdot \left(\alpha \vec{U}\vec{U}\right) = -\alpha \nabla \frac{P}{\rho_f} - \vec{R}_{sl} - \nabla \cdot \vec{\vec{\tau}} \tag{2.6}$$

In these equations, α is the volumetric fraction of fluid, $\vec{U}$ is the flow velocity, P is the pressure, ρ_f is the fluid density, $\vec{R}_{sl}$ is the drag force from the immersed particles and $\vec{\vec{\tau}}$ is the stress tensor for a Newtonian fluid.

Another approach to model fluidized beds is using an Euler-Euler scheme, where the particles are modeled as another fluid and the Navier-Stokes equations for two immiscible fluids are solved. For this it is necessary to define a granular bulk and shear viscosity and a granular pressure to completely define the behavior of the solids. Ding and Gidaspow (1990) have proposed a model derived from the Boltzmann equation for the velocity distribution of particles for example.

The described approach works best with many particles in the system so that it can be considered homogenous in the bed scale. But it has problems with narrow beds in which the size of the particles is comparable to the bed and using the fluid approximation can not represent the discontinuities in the contact between particles. For these cases an Euler-Lagrange approach is better, representing each particle individually as explained in the next section.

2.2.3 Discrete Element Method

The DEM numerical simulations follow each particle in a Lagrangian frame solving the collisions and accompanying their trajectory. For this, the LIGGGHTS (Kloss *et al.*, 2012) code was employed in this thesis, which solves the equations of linear (Eq. 2.7) and angular (Eq. 2.8) momentum calculated to each particle per time step.

$$m_p \frac{d\vec{U}_{p,i}}{dt} = -V_p \nabla P + V_p \nabla \cdot \vec{\vec{\tau}} + m_p \vec{g} + \sum_j \vec{F}_{c,i,j} + \sum_w \vec{F}_{c,i,w} - V_p \vec{F}_{p,f} \tag{2.7}$$

$$I_p \frac{d\vec{\omega}_i}{dt} = \sum_j \vec{T}_{p,i,j} + \sum_w \vec{T}_{p,i,w} \tag{2.8}$$

In which the contact force between particles ($\vec{F}_{c,i,j}$) and between particle and wall ($\vec{F}_{c,i,w}$) is calculated using the Hertz model (Eq. 2.11) and the respective torques ($\vec{T}_{p,i,j}$ and $\vec{T}_{p,i,w}$) are calculated with the tangent component of the contact forces. P is the fluid pressure field, m_p is the particle mass, $\vec{U}_{p,i}$ is the velocity of the i-th particle, V_p is the volume of the particle, $\vec{g}$ is the gravity acceleration, $\vec{F}_{p,f}$ is the drag force per volume and I_p is the moment of inertia of the particle.

This kind of numerical simulation has been used to model the angle of repose of quasi-two-dimensional granular piles based on the measured friction coefficient of the particles with themselves and with the walls (Li *et al.*, 2005), calculate the discharge rate of particles in tubes (Li *et al.*, 2017a) and model the formation of craters due to the impact of granular projectiles (Carvalho *et al.*, 2023). These applications do not consider the interaction of the granular matter with fluids, for this it is necessary to define models for the definition of the solid surfaces as presented in the next section.

2.2.4 Immersed boundary model

There are two approaches to solve the coupling of a fluid flow in the presence of solid particles: the methods of resolved and unresolved surface. The first models the flow around each particle, which should be larger than multiple cells of the mesh, and sum the forces of contact to calculate the particles' movement and the changes in the flow. The second uses fluid cells larger than the particles, using the solid volumetric fraction (ratio of the volume occupied by particles by the total volume analyzed) and experimental models to calculate the effects of the solids in the flow. Those differences can be seen in the Figure 2.4.

To model narrow fluidized beds, one can use the unresolved immersed boundary model with particle fraction calculated through the method "big Particle" (Goniva *et al.*, 2012), which sets the fluid fraction to 0 in every cell whose center lies inside a particle and creates a rough contour of the solids. Even though it does not simulate completely the flow around each particle, it is computationally cheaper than a resolved simulation and allows the execution of tests faster. The adoption of this model is common to similar works (Cúñez; Franklin, 2019), specially because of the advantages of using a two phase model in the fluid equation through an artificial porosity in the representation of the beads.

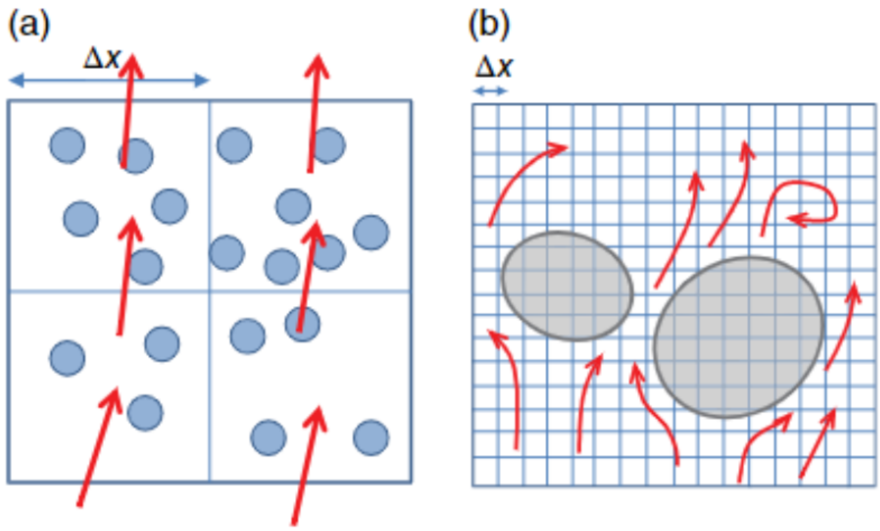

Figure 2.4 – Differences in the mesh used with the (a) unresolved and (b) resolved immersed boundary models, reproduced from Norouzi *et al.* (2016)

.

A different model to tackle the issue of having particles bigger than the CFD cell is called "divided", in which each particle is divided in 29 regions and the centroid of each one represents its volume to calculate the solid fraction on the CFD cells. Therefore, the particle's volume can be divided into multiple CFD cells and this is useful when particle's diameter is close to the size of the mesh cells (Goniva *et al.*, 2012). Another important model to define in the simulation is the behavior of solids collision, presented in the next section.

2.2.5 Collision models

There are many models to calculate collisions in DEM simulations, as the study of contact between elastic spheres is complicated depending on the history of loads imposed (Mindlin; Deresiewicz, 1953). The Hertz and Hooke models are available in the simulation software, both are based in defining the elastic constants (k) and viscous dissipation (γ) in the normal (n) and tangent (t) directions (Eq. 2.9).

$$\vec{F_c} = (k_n\vec{\delta_n} - \gamma_n\vec{v_n}) + (k_t\vec{\delta_t} - \gamma_t\vec{v_t}), \text{ tangent force limited by } F_t \leq x_\mu F_n \qquad (2.9)$$

In which x_μ is the static friction coefficient. The models differ in the definition of the elastic and viscous dissipation constants, Hooke's model is described in Equations 2.10 and Hertz's in Equations 2.11. To keep simplicity, the constants are described in the nomenclature.

$$k_n = k_t = \frac{16}{15}\sqrt{R^*}Y^*\left(\frac{15m^*U_p^2}{16\sqrt{R^*}Y^*}\right)^{1/5}$$
$$\gamma_n = \gamma_t = \sqrt{\frac{4m^*k_n}{1+(\pi/ln(e))^2}} \tag{2.10}$$
$$k_n = \frac{4}{3}Y^*\sqrt{R^*\delta_n},\ k_t = 8G^*\sqrt{R^*\delta_n}$$
$$\gamma_n = -2\sqrt{\frac{5}{6}}\psi\sqrt{S_n m^*},\ \gamma_t = -2\sqrt{\frac{5}{6}}\psi\sqrt{S_t m^*} \tag{2.11}$$

It is worth noticing that CFD-DEM simulations results are not affected much by changes in the elastic modulus (Tsuji *et al.*, 1993; Müller *et al.*, 2008). Because of this, it is common to use lower elastic modulus compared to the real materials to allow for larger time steps in the calculations. Burns *et al.* (2019) observed the effects of particle's mass, collision velocity, damping coefficient and elastic modulus. In particular, they reported that simulations with softer spheres are stable with larger time steps and proposed a linearized stability criteria $\Delta t \leq 2m_p/\gamma_n$, as well as a nonlinear map analysis presented in the work.

Other popular choices to estimate the maximum time step to a stable DEM simulation are the Rayleigh and the Hertz criteria. Analyzing the Rayleigh waves propagating in the surface the critical time step $\Delta t = \frac{\pi R_p}{\zeta}\sqrt{\frac{\rho_p}{G}}$ can be determined (Li *et al.*, 2005; Burns *et al.*, 2019), where R_p is the particle radius, G is particle shear modulus and $\zeta \approx 0.8766 + 0.163\nu$ is a function of the Poisson ratio (ν) (Johnson, 1985). The Hertz criteria is based on the eigenvalue calculation of the differential equations representing the dynamics of the contact.

Lastly, another model of interest chosen in the numeric simulations is the drag interaction between particles and fluid, as presented in the next section.

2.2.6 Drag models

An important step to CFD-DEM simulations is the definition of the drag model. If the unresolved immersed boundary model is used, the models of Ergun (Ergun, 1952), DiFelice (Felice, 1994), Beeststra (Hoef *et al.*, 2005) and Gidaspow (Gidaspow, 1994) can be used, the last is presented in Equation 2.12.

$$\vec{F}_{p,f} = \frac{1}{V_{cell}}\sum_{i=0}^{N}\frac{V_{p,i}\beta}{1-\alpha}\left(\vec{U}_f - \vec{U}_{p,i}\right) \tag{2.12}$$

In which V_{cell} is the volume of fluid cell in this calculation, $V_{p,i}$ is the volume of the i-th particle, $\vec{U}_f$ is the average fluid velocity, $\vec{U}_{p,i}$ is the velocity of the i-th particle and β is the coefficient of momentum exchange between the phases due to drag force, calculated as shown in the Equation 2.13.

$$\beta_{Gidaspow} = \begin{cases} 150\frac{(1-\alpha)^2\mu_a}{\alpha d_p^2} + 1,75\frac{\rho_f|\vec{U}_f-\vec{U}_p|(1-\alpha)}{d_p} & ,\alpha < 0,8 \\ \frac{3}{4}C_d\frac{\rho_f\alpha(1-\alpha)|\vec{U}_f-\vec{U}_p|}{d_p}\alpha^{-2,65} & ,\alpha \geq 0,8 \end{cases} \tag{2.13}$$

In which C_d is the drag coefficient related to the Reynold's number of the particles $Re_d = \frac{\rho_f\alpha d_p|\vec{U}_f-\vec{U}_p|}{\mu_f}$ presented in Equation 2.14.

$$C_d = \begin{cases} \frac{24}{Re_d}(1+0,15(Re_d)^{0,687}); Re_d < 1000 \\ 0,44; Re_d \geq 1000 \end{cases} \tag{2.14}$$

The DiFelice model (Felice, 1994) is also presented in Equation 2.15, and the different approach to calculate the coefficient of momentum exchange using a function of the bed voidage (α). Using this correlation over the Gidaspow model has an advantage of using a single equation to all Reynolds numbers.

$$\beta_{DiFelice} = \frac{3}{4}\left(0.63 + \frac{4.8}{\sqrt{Re_d}}\right)^2 \frac{\rho_f(1-\alpha)|\vec{U}_f - \vec{U}_{p,i}|}{d_p}\alpha^{-\chi} \tag{2.15}$$

In which the exponent of the voidage function is $\chi = 3.7 - 0.65\exp[\frac{-(1.5-\log_{10}(Re_d))^2}{2}]$. Agrawal *et al.* (2018) compared different models in a pseudo-2D fluidized bed and concluded that, from the two presented models, the DiFelice model is more accurate considering average bed height, particle velocities and granular temperature. Following the description of modelling the behavior of narrow fluidized beds, it is important to review the main quantities that can be calculated from bed observation and are used to characterize the system as detailed ahead.

2.3 Characterization of fluidized beds

The extensive study of fluidization consolidated a few classic measurements used in the field to classify and understand different patterns observed in the experiments. These quantities are presented and explained in the following sections.

2.3.1 Granular temperature

Among the measurements that can be performed to better understand the behavior of fluidized beds is the granular temperature. It comes from an analogy of the motion of individual particles with gas molecules, and can be used to analyze the anisotropies of the bed and the stresses caused by the solids (Tartan; Gidaspow, 2004; Jung *et al.*, 2005).

The calculation of granular temperature (θ) is based on the mean deviation of average particle velocity. In a specific region of space with N particles, the average particle velocity $\langle \vec{U}_p \rangle$ can be expressed by Equation 2.16, and granular temperature is the component average of the velocity deviation squared, as in Equation 2.17.

$$\langle \vec{U}_p \rangle = \frac{1}{N} \sum_{i=1}^{N} \vec{U}_{p,i} \tag{2.16}$$

$$\theta = \frac{1}{N} \sum_{i=1}^{N} \frac{1}{3} \sum_{j=x,y,z} [U_{p,ij} - \langle U_p \rangle_j]^2 \tag{2.17}$$

This measurement was used by Cúñez and Franklin (2020a) to identify crystallization and jamming in narrow fluidized beds via a reduction of granular temperature caused by the decrease in particle agitation.

2.3.2 Particle mixing and segregation

There are several measurements of mixing for particulate materials, as it is often a requirement in chemical or pharmaceutical industries to mix different powders. The Lacey index (Lacey, 1954) is calculated by sampling the concentration of a tracer particle (or one solid type in a binary mixture) in various defined locations of the material and computing the variance of this concentration S^2. It is then compared with the variance of the completely segregated case S_0^2 and the variance of the completely mixed case S_R^2 to obtain the Lacey mixing index M_{Lacey} as in Equation 2.18.

$$M_{Lacey} = \frac{S_0^2 - S^2}{S_0^2 - S_R^2} \tag{2.18}$$

Another measurement to monodisperse beds is the tracing-counting method (Liu *et al.*, 2020; Liu; Chen, 2010; Hernández-Jiménez *et al.*, 2018; Oke *et al.*, 2016) based on the division of the bed in B vertical regions (placed side by side horizontally) and coloring half the bed a different color to act as a tracer in the experiments, as seen in Figure 2.5. The mixing evolution with time can then be understood by the change of the standard deviation of tracer concentration in the regions $C_i(t)$ (Eq. 2.19).

$$S(t) = \sqrt{\frac{1}{B}\sum_{i=1}^{B}[CT_i(t) - \langle CT\rangle(t)]} \quad (2.19)$$

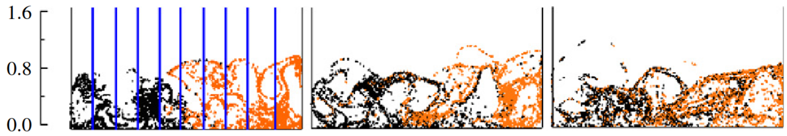

Figure 2.5 – Example of calculation of mixing in fluidized beds by coloring half of the particles and observing the evolution of the tracer concentration in horizontally organized regions, numerical simulation snapshots reproduced from Liu and Chen (2010).

Where, $\langle CT\rangle(t) = \frac{1}{B}\sum_{i=1}^{B} CT_i(t)$ is the average concentration of tracers in all regions. Zhang *et al.* (2009) used a similar approach to analyze mixing in a spouted bed, but divided the images in a grid of cells with both horizontal and vertical divisions and used the standard deviation (Eq. 2.19) divided by the average tracer concentration as the mixing index.

Hernández-Jiménez *et al.* (2018) also proposed a different index to accommodate their specific experimental setup, in it the bed is divided in cells and the average number of cells occupied by solids is calculated as N_{total}. For each cell with solids, it is labeled as "mixed" if the relative difference between the volumetric fraction of different species is smaller than a threshold, the total number of "mixed" cells is N_{mixed}. The ratio of the counts (Eq. 2.20) fluctuates around 1 for a completely mixed bed due to instabilities propagating through the tube that change the number of cells with solids present, and this measurement was proposed as a suitable mixing index $M_{Hernadez}$ for the experiments presented.

$$M_{Hernandez} = \frac{N_{mixed}}{N_{total}} \quad (2.20)$$

It is worth highlighting the multiplicity of possible mixing index calculations because each measurement is better suited to analyze the experiment it was developed for.

3 EXPERIMENTAL METHODOLOGY

3.1 Introduction

To investigate the dynamic of a narrow fluidized bed, experiments were conducted in a glass tube with Inner Diameter (ID) of $3\,\mathrm{mm}$ and compared with numerical simulations to provide a better understand of the solids' movement. Furthermore, the bed can be inclined to predetermined angles which lead to interesting new phenomena being observed.

The following parameters were varied in the physical experiments:

- Mean flow velocity at entry (U_e)
- Particle's material (glass and zirconium)
- Angle of the bed with respect to the gravity direction (φ)
- Number of particles (N)

In the following sections, the experimental and numerical setups will be detailed. First the experiments and data analysis are explained, and then the numerical simulations are presented with details about the setup to mimic the observed results. Parts of this section have been published in the work "Bidisperse micro fluidized beds: Effect of bed inclination on mixing" by the author and the advisor (Oliveira; Franklin, 2024).

3.2 Physical experiments

3.2.1 Experimental setup

The bed is made using a glass tube (ID = $3\,\mathrm{mm}$) secured to an aluminum extrusion that can pivot at the top and is secured in position by a pin and a perforated steel plate (this allows for the operation of the bed in different angles relative to the gravity direction: 0°, 15°, 30°, 45° and 60° with uncertainty of ± 0.5°), a diagram of the complete setup can be seen in Figure 3.1 and the detail of the pivoting system in Figure 3.2. The air used to fluidize the particles is supplied via a tank of compressed air, the pressure is kept by a compressor up to $120\,\mathrm{psi}$. The volumetric flow rate (Q) is monitored by a rotameter (with gradation of $5\,\mathrm{L\,h^{-1}}$

that correspond to an uncertainty of $0.2\,\mathrm{m\,s^{-1}}$ in the average air velocity in the tube) and is used to calculate the superficial velocity (U_e) of the air in the tube with Equation 3.1.

$$U_e = \frac{4Q}{\pi D^2} \tag{3.1}$$

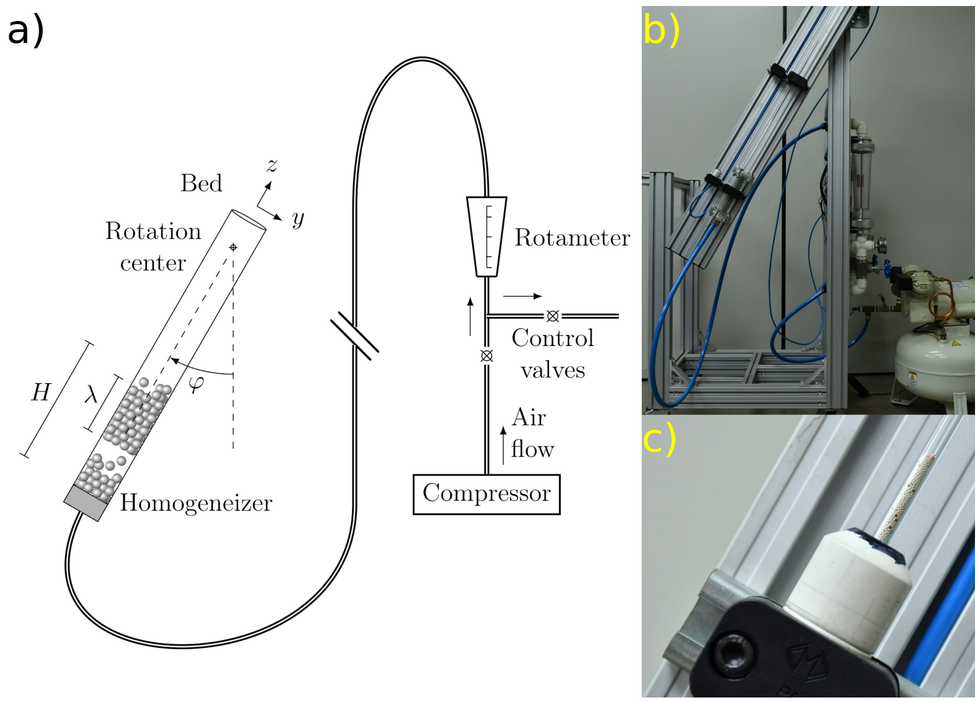

Figure 3.1 – (a) Diagram of the fluidized bed setup, (b) picture of the experimental bench and (c) a detail of the fluidized bed with the particles, from Oliveira and Franklin (2024)

The glass and zirconium particles used in the experiments are show in Figure 3.3. The beads were chosen because of the high sphericity and their diameter is between $0.4\,\mathrm{mm}$ and $0.6\,\mathrm{mm}$ that fits in the narrow tube used but are still big enough to be tracked in the movies of the camera and characterize a very-narrow fluidized bed. Furthermore, both beads can be classified as type D in the Geldart classification (Geldart, 1973), which means they form spouted beds easily.

For each run, the chosen mass of particles is weighted in a precision scale. The zirconium particles are placed in the tube followed by the glass beads, the bed is then fluidized in the vertical position until steady layer segregation is observed. The researcher inclines the stratified bed to the desired position, the camera starts to record, and the air flow is imposed keeping the volumetric flux constant in the rotameter using the valves. The high speed camera records the experiments for about $30\,\mathrm{s}$, except in the cases that a fixed bed condition is observed

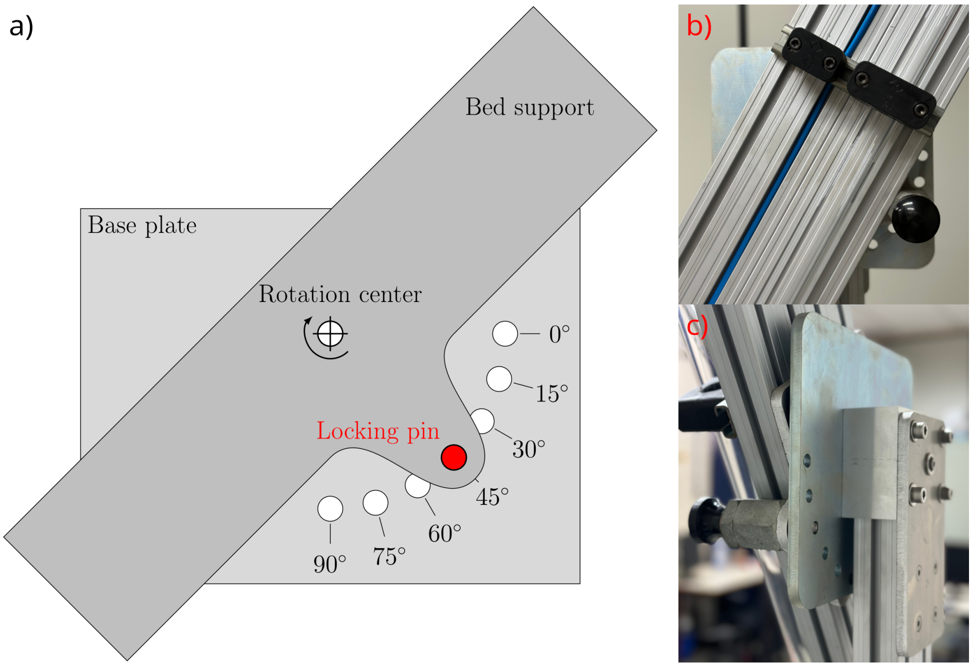

Figure 3.2 – (a) Diagram of the pivoting system used in the experiments, (b) a picture of the front view and the handle used to operate the system and (c) a picture of the back of the plate and the perforations, from Oliveira and Franklin (2024)

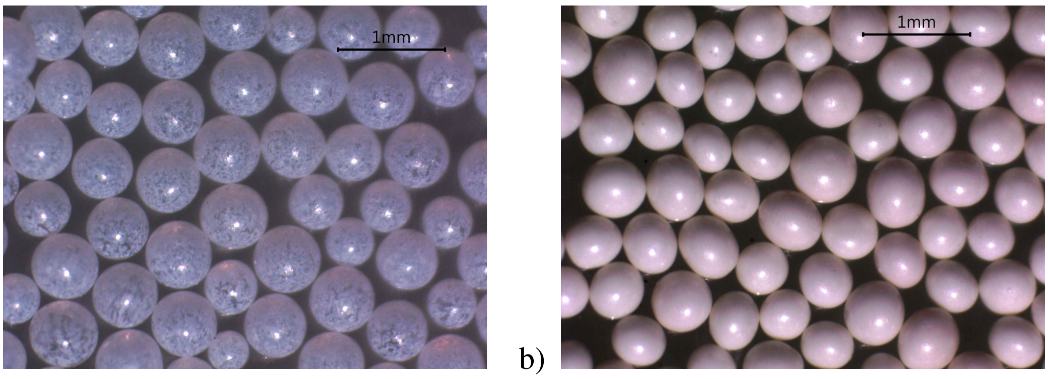

a) b)

Figure 3.3 – Microscope photography of the (a) glass and (b) zirconium spheres used in the experiments, both particle types have a diameter between $0.4\,\mathrm{mm}$ and $0.6\,\mathrm{mm}$, from Oliveira and Franklin (2024).

and the run stops earlier. This same setup can be used to perform other runs with different inclinations and average flow velocities following the same steps. To change the mass of particles, the researcher extracts the particles from the tube by the top, because the bottom is blocked by the flow homogenizer, and places the selected masses for the next run. The first $5\,\mathrm{s}$ were removed from the analysis to avoid the initial velocity ramp until a steady air flow velocity is achieved.

The experiments were recorded using a high speed camera Phanton VEO-E 340L fitted with a CMOS (Complementary Metal-Oxide-Semiconductor) sensor, which was set to a frame rate of $1000\,\mathrm{Hz}$ and a $60\,\mathrm{mm}$ F/2.8 fixed lens aligned parallel to the rotation axis of the bed was used to improve image quality and light gathering capacity compared to the other slower zoom lens available. The maximum resolution of the Phantom camera is 2560 px x 1600 px at $800\,\mathrm{Hz}$, but the Region Of Interest (ROI) was fixed at 2560 px x 128 px due to the narrow profile of the bed which allows the use of a higher capture frequency. To use the desired camera settings, the bed was illuminated by LED (Light Emitting Diode) lamps connected to a continuous current supply, which provided a steady light supply bright enough to record the particles with a lower exposure time.

In the experiments presented in the Table 3.1 the mass of glass (m_g) and zirconium (m_z) beads was varied, as well as the cross-sectional mean air velocity ($\bar{U}$). In the table the height of the bed and mean air velocity at the condition of incipient fluidization are also presented, and the Reynolds numbers based on the mean velocity of the air flow ($\bar{U}$) and the tube's ID (Re_D) and on the particles' diameter (Re_d). The stokes number based on the particles' terminal velocity (St_t) was also calculated as $St_t = 2.86 \times 10^4$ and 6.44×10^4 for the glass and zirconium particles respectively, following Equation 3.2.

$$St_t = \frac{U_{p0} d \rho_p}{9 \mu_f} \tag{3.2}$$

In Equation 3.2 the settling velocity U_{p0} of a single particle is estimated using the Richardson-Zaki correlation (Eq. 2.1) with $n = 2.4$ as 0.70 and $0.96\ \mathrm{m\,s^{-1}}$ for glass and zirconium respectively. The solid volumetric fraction is considered $\phi \approx 0.5$ following the work of Cúñez and Franklin (2020a). Furthermore, the incipient fluidization condition is estimated by the inception of particle movement observed in the images (Zhang *et al.*, 2021), and it is used to approximate minimum fluidization (Cúñez; Franklin, 2020a; Oliveira *et al.*, 2023; Cúñez; Franklin, 2023). There might be a difference between the velocities of minimum (U_{mf}) and incipient fluidization (U_{if}) due to high friction with the walls and adhesion forces acting on the grains, this leads to a large fluidization-defluidization hysteresis and a discrepancy with correlations developed for larger beds (Zhang *et al.*, 2021). For bidisperse beds the incipient fluidization is measured by the onset of movement on the top layer following the work of Formisani *et al.* (2008).

Table 3.1 – Parameters of the tests carried: mass of glass m_g and zirconia m_z particles, fluid velocity for incipient fluidization U_{if} and the bed height at this condition h_{if}, cross-sectional mean velocity normalized by the incipient velocity $\bar{U}/U_{if}$ and the Reynolds number for the tube Re_D and for the particles Re_d based on the cross-sectional mean velocity. Each case was carried out with the inclinations φ = 0°, 15°, 30°, 45° and 60°.

Case	m_g	m_z	U_{if}	h_{if}	$\bar{U}/U_{if}$	Re_D	Re_d
...	g	g	m/s	mm	...	...	...
1	0.3	0	0.63	24	2.5	311	52
2	0.3	0	0.63	24	2.8	350	58
3	0.5	0	0.63	41	2.5	311	52
4	0.5	0	0.63	41	2.8	350	58
5	0.7	0	0.63	56	2.5	311	52
6	0.7	0	0.63	56	2.8	350	58
7	0.2	0.4	0.63	36	2.5	311	52
8	0.2	0.4	0.63	36	2.8	350	58
9	0.2	0.5	0.63	41	2.5	311	52
10	0.2	0.5	0.63	41	2.8	350	58
11	0.2	0.7	0.78	51	2.0	311	52
12	0.2	0.7	0.78	51	2.3	350	58
13	0.3	0.4	0.71	44	2.2	311	52
14	0.3	0.4	0.71	44	2.5	350	58
15	0.3	0.5	0.78	49	2.0	311	52
16	0.3	0.5	0.78	49	2.3	350	58
17	0.3	0.7	0.78	59	2.0	311	52
18	0.3	0.7	0.78	59	2.3	350	58
19	0	0.9	1.58	26	1.25	389	65
21	0	0.9	1.58	26	1.38	428	72
22	0	1.2	1.73	46	1.05	350	58
23	0	1.2	1.73	46	1.14	389	65

Despite the best efforts in the assembling and preparation of the experiments, the temperature of the room is always between 21 and 23°C and relative humidity is between 46% and 77%, the cases 19 to 23 were affected by electrostatic charge accumulating in the particles and tube. That prevented the fluidization of the bed and therefore these runs could not be used in this work. Nevertheless, previous works show that the particle density do not affect the plugs' length and celerity (Cúñez; Franklin, 2020a). Therefore, the results of glass particles are representative of monodispersed beds.

With this setup, it was obtained a series of grayscale images for each experiment listed in the Table 3.1, these pictures allowed the visualization of the front layer of particles and their movement can be calculated as presented in the next section.

3.2.2 Data analysis

The images recorded were preprocessed with a bilateral filter to smooth the noise without loosing detail in the particles' borders. Due to the dark background used in the recording process and the high contrast of the white particles there was no need to subtract the background. Calibration frames were used to establish the scale of the images, a C++ program was developed to automatically detect the left and right edges of the bed as well as the bottom and determine the ratio of pixels per mm, which was within 12 and 22 px/mm. The detection is performed sweeping the image from left to right looking for large changes in the brightness sum of all pixels in each column, and the greatest positive change is the left border while the greatest negative change is the right border.

These images with only the region of interest can be placed side-by-side forming a spatio-temporal diagram. Often it is necessary to skip frames if the interest is to observe slower events, and the ideal frequency of frames for each type of instability was chosen by the author testing different configurations. The author wrote a C++ code (Oliveira; Franklin, 2023) that can be compiled in a tool which produces the diagrams automatically for the given parameters.

The height of the bed was measured finding the bright pixel (with a brightness value above a given threshold, chosen to detect particles from the background) that was the furthest distance from the bottom and calculating its vertical position by the number of pixels to the bottom of the bed. And, to find the visible particles, local maxima were marked and those which coincided with a bright area and had a consistent distance to local minima and dark pixel were marked as particles, as seen in the Figure 3.4. This approach gives consistent results, finding all visible particles with few false positives that are cleaned in the following steps of processing.

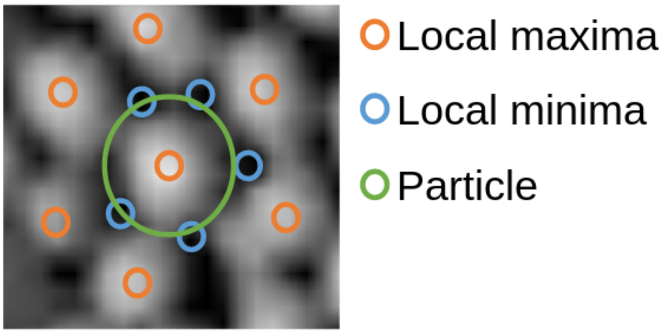

Figure 3.4 – Method to identify particles in the micro fluidized bed images, from Oliveira and Franklin (2024)

To follow each visible particle's movement, a system of labels was implemented assigning a tag to the particles in the first frame and, using an auction algorithm (Bertsekas, 1992) it is possible to follow the particles' positions in each frame by minimizing the total distance traveled in the bed by all particles. New particles are assigned new labels and a few particles are lost, so the tags are closed, and this process repeats to all recorded frames. To improve precision, the tracking program also implements a Kalmann filter to locate particles that were not recognized in a single frame for any imprecision in the identification process. The few lost particles are to be expected as they can move away from the camera and be covered by others, this does not hinder the results as the main interest is the general movement in the whole bed. In the bidisperse cases, the types of particles were identified by their average brightness, as the zirconium particles appear brighter than the glass ones in the images.

Together with the lagrangian approach of following the individual grains, an eulerian method is used as well, by saving snapshots of velocity fields and granular temperature (θ) (Eq. 3.3) across the bed. Figure 3.5 show a representation of a cell in which the bed is divided for the presented measurements. A flux of particle in terms of area ($\vec{A}$) is also calculated with Equation 3.4, which is based on the work of Jiang *et al.* (2018) and is used to visualize the mean movement of solids in the bed.

$$\theta = \frac{1}{2}\sum_{k=y,z}\frac{1}{N_{cell}}\sum_{i=1}^{N_{cell}}\left(U_{p,ki} - \langle U_p\rangle_k\right), \text{with } \langle U_p\rangle_k = \frac{1}{N_{cell}}\sum_{i=1}^{N_{cell}} U_{p,ki} \tag{3.3}$$

$$A_k = \frac{1}{l_k} \sum_{i=1}^{N_{cell}} [U_{p,ki} \pi r_i^2] \text{ , with } k = y, z \tag{3.4}$$

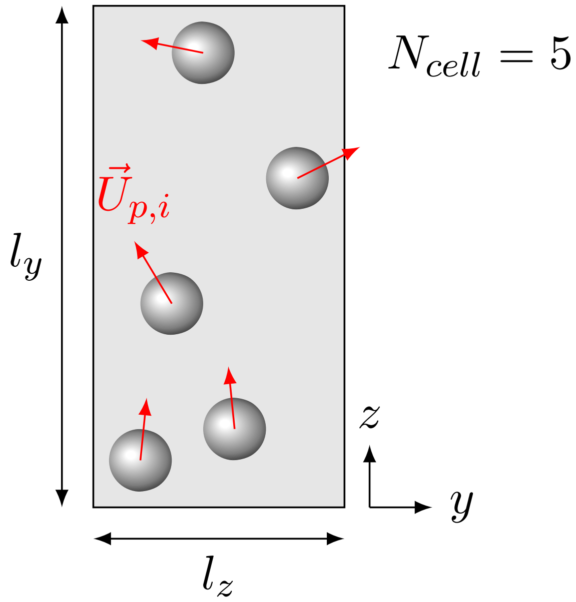

Figure 3.5 – Example of a cell in which the granular temperature and area flux are calculated, from Oliveira and Franklin (2024)

With the area flux of particles, the bed moment (L) is proposed as a measurement of the tendency of solids to circulate inside inclined fluidized beds (Eq. 3.5). The center of rotation is calculated searching by the central area with less average solid movement in the bed. And the bed moment (L) is the sum across all B cells, in which the bed is divided, of the cross product between the distance from the center of rotation ($\vec{r}$) and the average area flux of particles ($\vec{A}$) as seen in Figure 3.6. The dot product with the direction of inclination aligns the measurement with the direction of interest producing a scalar result that can be used to compare the tests. This decision was inspired by calculation of the torque of a solid body subject to multiple forces, and is used to explore the mixture of solids in the bed.

$$L = \sum_{i=1}^{B} \left[\vec{r} \times \vec{A} \right] \cdot \hat{e}_x \tag{3.5}$$

Furthermore, the size of the mixing layer in the bidisperse fluidized beds (Fig. 3.7) is also defined in Equation 3.6, the number of particles in each region are defined in the Figure 3.7. This was proposed as an alternative to usual measurements presented in the literature review to avoid errors due to the low number of particles and the instabilities propagating in the

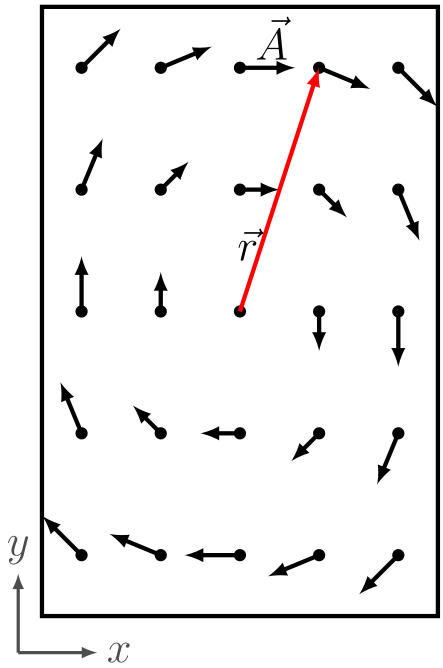

Figure 3.6 – Calculation of the angular moment, which is defined to represent the circulation of solids in the bed, from Oliveira and Franklin (2024)

fluidized bed and can be seen in Figure 3.7. The regions surrounding the particles of the same type can be convex to avoid representing sliding motion as mixing, which are two different regimes observed inclining further the tube, but it is limited to $90°$ as the minimum external angle to avoid jagged boundaries.

$$M = \frac{P_{21} + P_{12}}{P_1 + P_2} \tag{3.6}$$

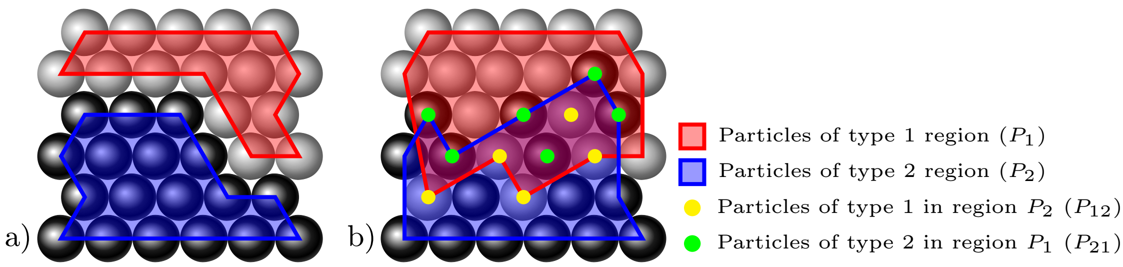

Figure 3.7 – Measurement of the mixture layer size developed to better represent the mixture observed in inclined fluidized beds, from Oliveira and Franklin (2024). The figure presents a comparison of (a) sliding motion and (b) mixing.

The plug-like instabilities length and celerity are computed with the spatio-temporal diagrams, using every available frame to improve the resolution in time of the measurements.

The diagram is blurred with a Gaussian noise in a 51 by 51 pixel kernel and the plugs are identified with a threshold filter that selects the regions with brightness values above 35% of the maximum. The plug length and number of plugs are calculated following a vertical line from the bottom of the bed and counting the number of bright regions and the number of pixels inside each region. If the length is below one tube diameter it is considered a false positive and the measure is disregarded, this process is repeated for the number of frames present in the diagram. To calculate the celerity, each plug is assigned a label and is compared to all plugs in the next frame above its current height (because plugs only move upwards), the one with the smallest distance receives the same label and the tracking continues. It is also necessary to delete labels when the plug reaches the top of the bed, breaks or merge with another, in the last case the label of the plug above is preserved. This process can be seen in Figure 3.8, where two plugs can be seen merging in the begging of the sequence and the smaller plug breaking up and joining the bottom of the bed in the right of the Figure.

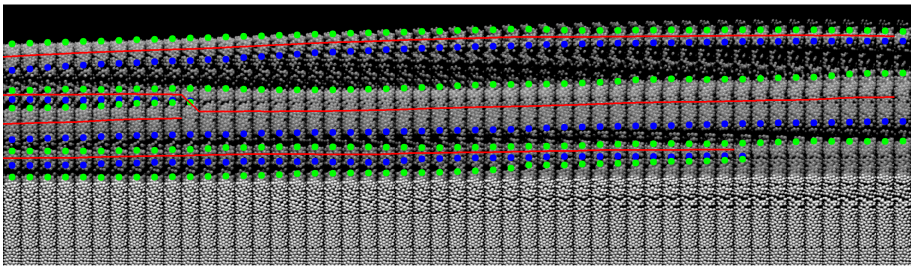

Figure 3.8 – Example of the results of the plug identification algorithm. Blue dots represent the top of the plugs, green dots the bottom and the red lines are the trajectory of the center of the plug.

All described measurements are implemented in a C++ code that can be compiled in a simple tool that reads a series of grayscale images, recorded following the procedure described in the beginning of the chapter, pre-process the images to a new folder and then perform the required computations and stores the results in plain text files. The results are further processed when necessary in Python™ notebooks that are also used to make the relevant graphics to understand the experiments. All codes are publicly available in Oliveira and Franklin (2023). These measurements were developed to understand the mixing of solids observed in inclined beds. And also used to validate the numerical simulations of the narrow fluidized bed presented in the next section.

3.3 Numerical simulations

The numerical simulations were conducted using the software CFDEM®coupling (Goniva *et al.*, 2012), which combines the packages OpenFOAM (Weller *et al.*, 1998) and LIGGGHTS® (Kloss *et al.*, 2012), performing the coupling, through the calculation of exchanged forces, of the CFD and DEM simulations.

3.3.1 Particles simulation

Every numerical setup begins with a DEM simulation of falling particles in a vertical tube to represent the initial condition of settled beads in the bed prior to fluidization, the only difference is the number and type of particles. The desired number of particles was generated in random positions and with a downward velocity of $1\,\mathrm{m\,s^{-1}}$ to reduce the settling time, as presented in Figure 3.9a. The particles' characteristics are presented in Table 3.2 and the diameter is randomly chosen between $0.48\,\mathrm{mm}$, $0.50\,\mathrm{mm}$ and $0.52\,\mathrm{mm}$ with probability of 10%, 80% and 10% respectively, chosen to represent the natural variation observed in the experiments.

Table 3.2 – Physical characteristics of the particles considered in the DEM simulations.

Parameter	Type I	Type II
Material	Glass	Zirconia
Young modulus Y $[\mathrm{GPa}]$	70	95
Density ρ $[\mathrm{kg\,m^{-3}}]$	2500	4100
Diameter d $[\mathrm{mm}]$	$0.48 - 0.52$	$0.48 - 0.52$
Poisson ratio ν $[-]$	0.21	0.34

The simulation end time was set to $0.3\,\mathrm{s}$, with a step of $0.01\,\mu\mathrm{s}$ appropriate to solve the collisions using the Hertz model. The restitution and friction coefficients between all particles and walls was considered 0.1 and 0.6 respectively, and an example result can be seen in the Figure 3.9b that is used to simulate micro fluidized beds with $0.5\,\mathrm{g}$ of glass particles in different inclinations and fluid velocities, which correspond to 1650 particles.

The CFD-DEM simulations of fluidization were performed using the correspondent result of the DEM simulations presented as an initial condition, and the DEM configuration were kept unaltered in the next steps.

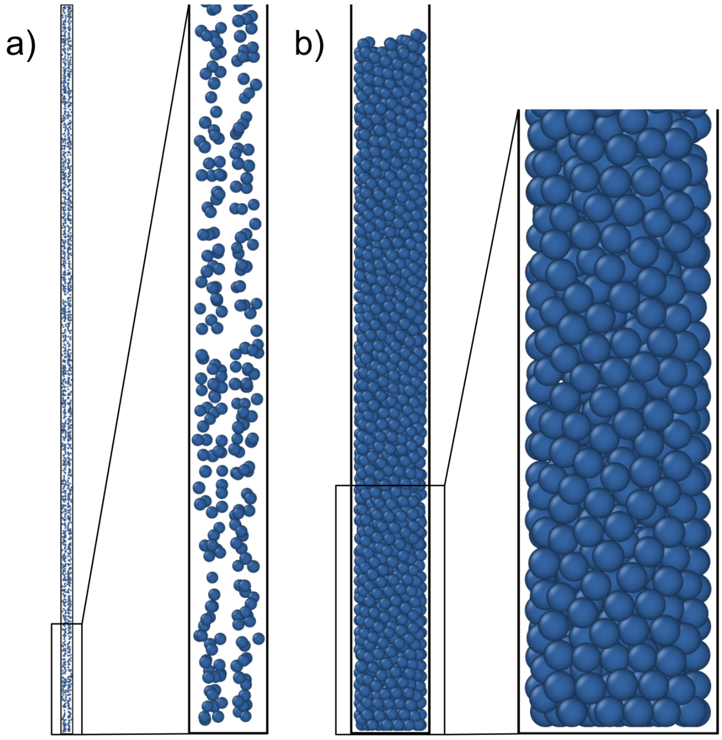

Figure 3.9 – (a) Example of an initial condition for the DEM simulation to form a fixed bed for the CFD-DEM simulations and (b) the result of the initial particle simulation to be used in the CFD-DEM simulations of inclined beds.

3.3.2 Fluid simulation

The CFD simulation is set up with the air parameters described in Table 3.3 and a mesh of 115200 cells divides the bed in cells small enough to properly represent the flow in the pipe and divide the particles for the unresolved method used in coupling, as seen in Figure 3.10. Furthermore, the tube walls have no slip boundary condition, the top surface a constant atmospheric pressure and the bottom inlet has a constant fluid velocity boundary condition, which is set to match the experimental data with an initial ramp of $0.1\,\mathrm{s}$ to avoid numerical instabilities in the start of the simulation.

Table 3.3 – Physical characteristics of the fluid in the CFD simulation

Parameter	Air
Density $[\mathrm{kg\,m^{-3}}]$	1.2
Kinematic Viscosity $[\mathrm{m^2\,s^{-1}}]$	1.5×10^{-5}

The time step to the fluid simulation is $1\,\mathrm{\mu s}$ and the results are stored every $1\,\mathrm{ms}$. The frequency of result storage is lower than the simulation itself to reduce the amount of generated data, the rate chosen is the same as the camera used in the experiments and can provide similar

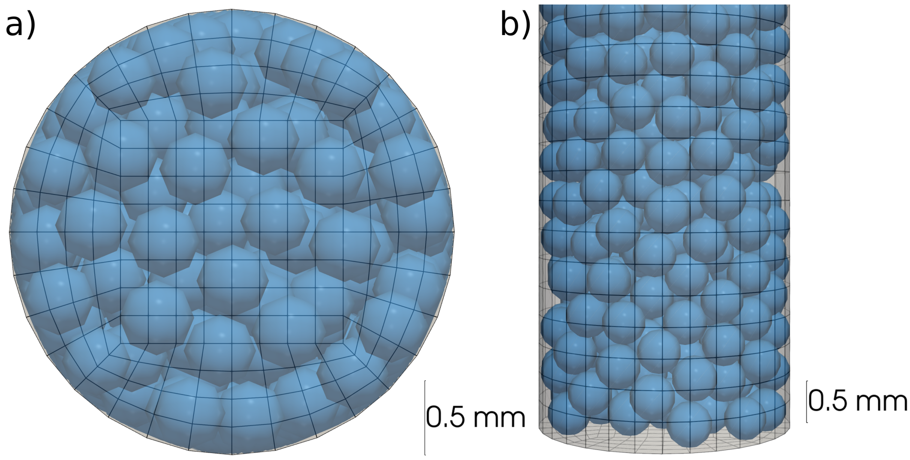

Figure 3.10 – (a) Bottom and (b) side view of the mesh used in the CFD numerical simulations compared to the particles in a fixed bed.

information to be compared, describing the individual motion of particles and general behavior of the micro fluidized bed.

3.3.3 Coupling

The coupling between the CFD and DEM simulations is executed with the DiFelice drag model and the void fraction is calculated with the "divided" model, which are explained in the literature review respectively in sections 2.2.6 and 2.2.4. The coupling time step is the same as the CFD simulation, $1\,\mu s$, this is the time interval between consecutive communications of the CFD and DEM simulations. The numerical simulations of $3\,s$ were carried in a computer with 10 physical cores and took $360\,h$ or appropriately 3600 CPU hours.

The first simulation results indicated that the method is not adequate to reproduce the experiments, which is clearly seen in the Figure 3.11. It presents the overshoot in bed height when compared to the experiments, despite the low restitution coefficient of 0.1 used in these runs, what indicated a missing physical effect which was not implemented in the numerical simulations.

The proposed missing effect is the presence of static charges in the particles and tube wall, which attracts the beads towards the walls and away from the center of the tube. This was indicated by particles stuck to the tube in the end of the experiments and suspended above the fixed bed when the air flow stops. Furthermore, other students in the group have reported similar issues using the same zirconium and glass particle in other experiments, and it is a known problem of gas-solid fluidized beds (Fotovat *et al.*, 2017).

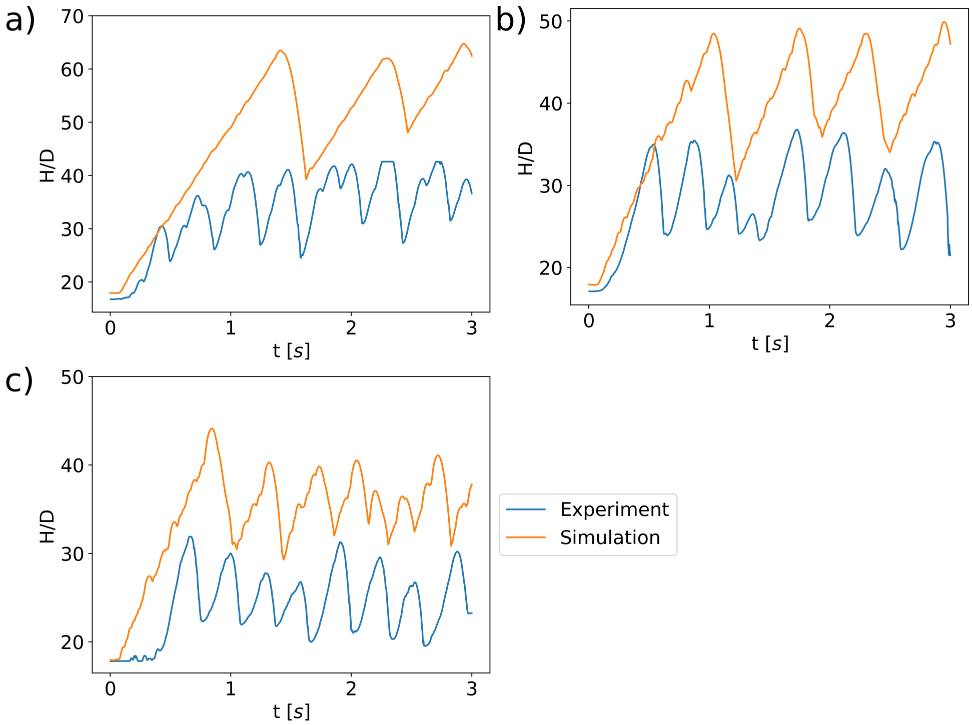

Figure 3.11 – Comparison of bed height H in the experiments and numerical simulations showing the discrepancy of the results and the incompatibility between model and experimental results with $0.5\,\mathrm{g}$ of glass particles, $\bar{U} = 1.57\,\mathrm{m\,s^{-1}}$ and inclination of $\varphi =$ (a) $0°$, (b) $15°$ and (c) $30°$

The CFDEM®coupling software used is unable to model the electrostatic charges build up and the Coulomb force acting on the particles, therefore a simplification is proposed in which a force normal to the wall is activated when the particles are close the wall. This can reproduce the main effects observed and is simpler to implement. Figure 3.12 shows the region close to the wall where the force is activated to simulate electrostatic attraction between the particles and the tube. This force is in the radial direction and is set to oscillate between zero and a maximum value to avoid trapping all particles in the wall, which is not observed in the experiments due to the dynamic oscillation of the charge in the solids.

Even this approach initially presented problems because every particle stuck to the wall forms a center channel for the air, similar to the crystallization observed in Oliveira *et al.* (2023), which is not observed in the experiments. The work of Fang *et al.* (2008) proposes an alternative by showing that the wall charge is inverted in the bottom of the bed. This last modification is implemented by inverting the direction of the forces displayed in the Figure 3.12 at the bottom of the bed, below the static bed height. This change improved the agreement of the simulations with the experiments and enabled the following analysis.

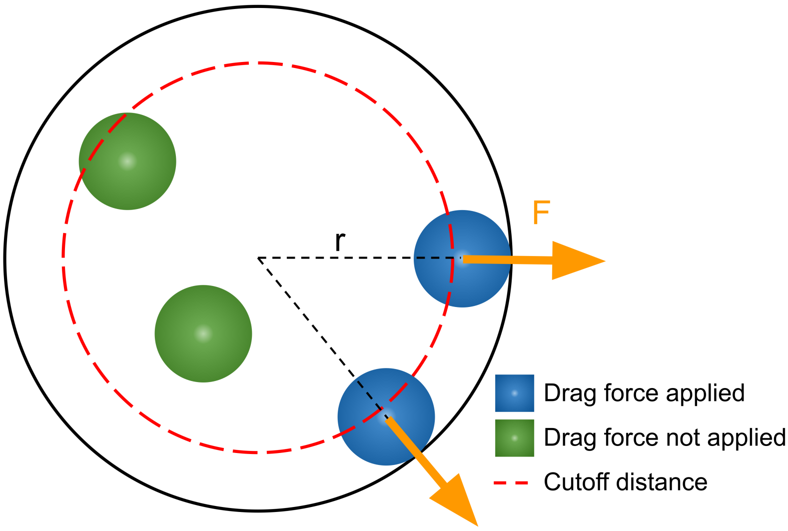

Figure 3.12 – Representation of the drag force used in the CFDEM®coupling to simulate electrostatic attraction between the particles and the tube wall, the force is radial and only acts close to the wall.

3.3.4 Data analysis

The numerical simulations save two types of results files, OpenFOAM presents fields of the flow properties per cell for each time step and LIGGGHTS saves each particle information. As expected from the simulation model, the outputs are fields for the fluid properties (like velocity, pressure and packing fraction) in an eulerian approach and per particle information (such as position and velocity) in a lagrangian approach.

Similarly to the experimental results, a C++ code is used to read the particle positions and velocities to calculate the bed height and eulerian fields for average particle velocity and granular temperature. Furthermore, the softwares ParaView (Ahrens *et al.*, 2005) and OVITO (Open Visualization Tool) (Stukowski, 2010) are used to create visualizations and diagrams to qualitative analysis.

4 RESULTS

Parts of this section have been published in the work "Bidisperse micro fluidized beds: Effect of bed inclination on mixing" by the author and the advisor (Oliveira; Franklin, 2024). In all sections the time averages exclude the beginning of the experiments to avoid the initial fluidization, while the air flux have not reached a steady value and the initial expansion is not representative of the steady state condition observed later. Unless stated otherwise, all averages are computed with the entire experiment run time.

4.1 Instability patterns

An approach to observe the behavior change when inclining the bed is analyzing spatio-temporal diagrams obtained placing snapshots of the micro fluidized bed side by side. Figure 4.1 shows four diagrams for different inclinations, and it is possible to see how the instabilities propagating in the tube gradually change from plugs and voids in the vertical case to superficial waves in the 45° and then a fixed bed condition is reached in the inclination of 60°. These changes are related to the formation of an air channel in the top of the bed for higher inclinations as investigated by O'Dea *et al.* (1990), that described a channeling regime in inclined fluidized beds. It also important to notice that the plugs only move upwards, then break up in the top of the bed and the particles descend in the bubble regions.

By comparing Figure 4.2 with 4.1 the effects of a higher fluidization velocity on the bed structure are visible. The most obvious change is the higher bed height compared to the slower gas velocity case. Beyond this, the instabilities transition to superficial waves or the fixed bed is delayed to higher inclinations (for example, the inclination of 45° in Figure 4.2 (d) still presents plug-like behavior which is not observed with lower fluid velocity).

This kind of instabilities are expected, as the particles used can be classified as type D in the Geldart classification (Geldart, 1973). These particles tend to form spouted beds that are subjected to large instabilities across the whole cross-section. Furthermore, the Froude number of the experiments is always high $Fr > 80$, which indicates particulate behavior in the Glasser *et al.* (1997) work. The bed is also in the aggregative region in the classification proposed by Liu *et al.* (1996) with discriminative number $Dn \approx 10^7$. These classifications are explained in the section 2.1.

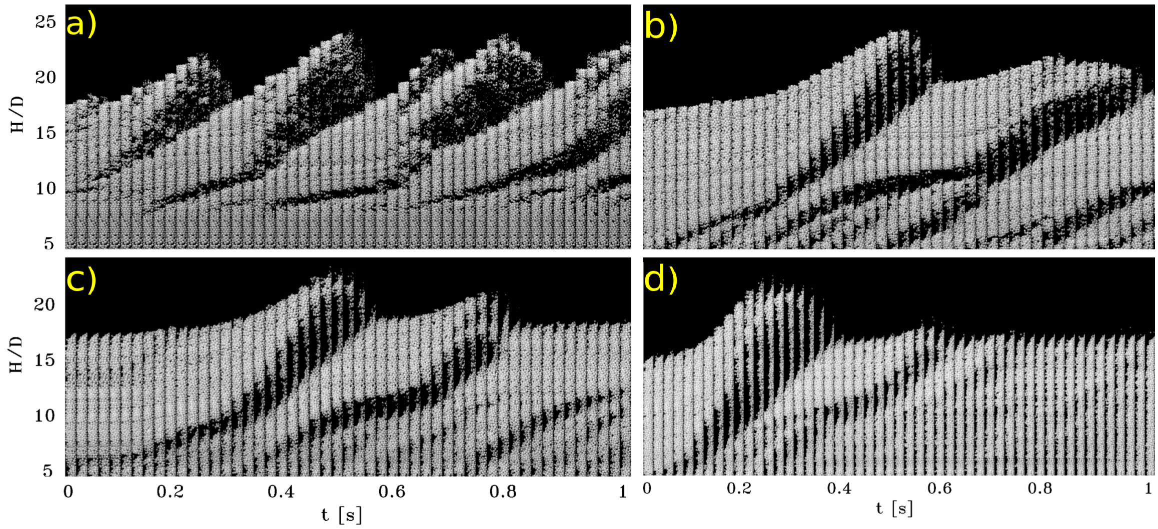

Figure 4.1 – Snapshots side by side of the case 3 in Table 3.1 with $m_g = 0.5\,\mathrm{g}$ (monodisperse bed) and $\bar{U}/U_{if} = 2.5$, for the inclinations $\varphi =$ (a) 0°, (b) 15°, (c) 30° and (d) 45°. The total time represented is $1\,\mathrm{s}$ with $20\,\mathrm{ms}$ of interval between the frames, reproduced from Oliveira and Franklin (2024).

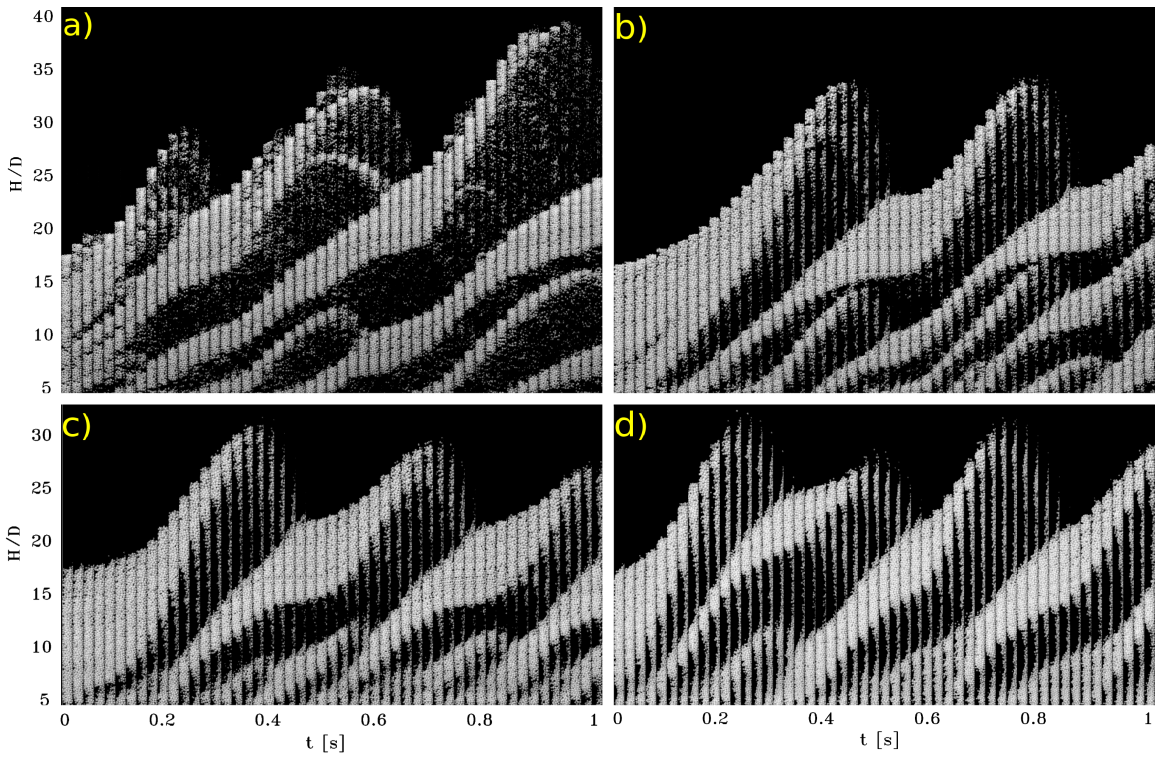

Figure 4.2 – Snapshots side by side of the case 4 in Table 3.1 with $m_g = 0.5\,\mathrm{g}$ (monodisperse bed) and $\bar{U}/U_{if} = 2.8$, for the inclinations $\varphi =$ (a) 0°, (b) 15°, (c) 30° and (d) 45°. The total time represented is $1\,\mathrm{s}$ with $20\,\mathrm{ms}$ of interval between the frames, reproduced from Oliveira and Franklin (2024).

In the bidisperse bed of Figure 4.3 the same behaviors of monodisperse beds are still present, with the transition from a plug regime to superficial waves and fixed bed. Beyond the similarities there is an important distinction in how the layers with each kind of particle behave. In vertical beds the particles organize in two distinct layers that remain separated for the duration of the experiments, but when inclination is introduced there is the formation of a mixing layer (as defined in Figure 3.7) with both kinds of particles between the monodispersed layers still present.

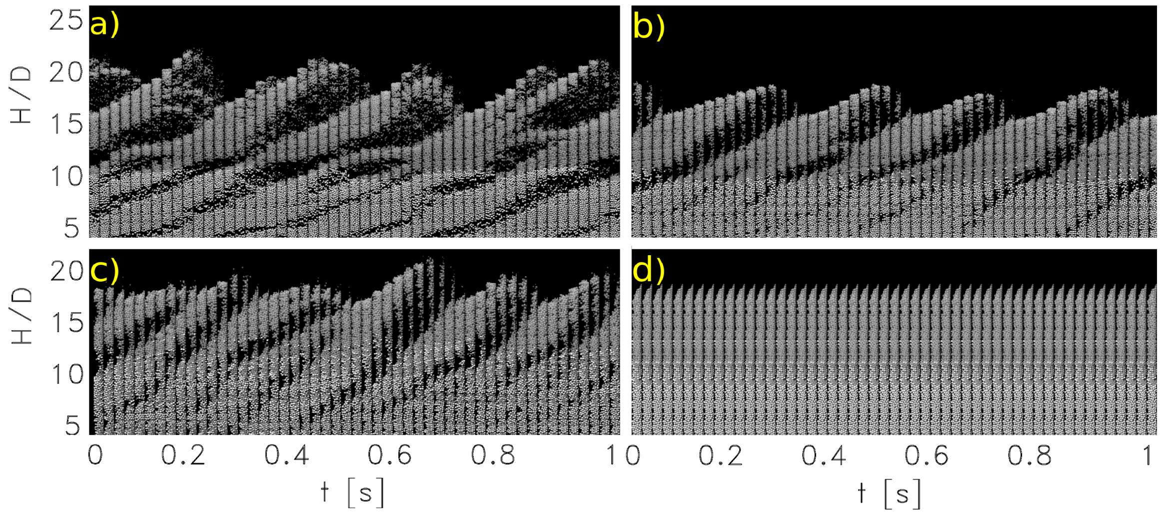

Figure 4.3 – Snapshots side by side of the case 10 in Table 3.1 with $m_g = 0.2\,\mathrm{g}$, $m_z = 0.5\,\mathrm{g}$ (bidisperse bed) and $\bar{U}/U_{if} = 2.8$, for the inclinations $\varphi =$ (a) 0°, (b) 15°, (c) 30° and (d) 45°. The total time represented is $1\,\mathrm{s}$ with $20\,\mathrm{ms}$ of interval between the frames, reproduced from Oliveira and Franklin (2024).

This mixing is observed only in intermediate inclinations, the vertical beds segregate the particles and higher inclinations lead to a fixed bed that impedes particle movement in general and also mixing by consequence. This phenomenon is explored further in the following section and a possible mechanism is presented and explained, as well as the plug instabilities present in the bed.

4.2 Effects of inclination on fluidization

To quantify the effects of inclining a micro fluidized bed, it is possible to start by investigating how the height of the bed changes with the angle. Figure 4.4 shows that the average bed height H decreases with an increase in the inclination angle φ, which agrees with the observations of Pozo *et al.* (1992) for small angles and regular beds. It is also possible to observe lower variation in the height indicate by smaller error bars that correspond to the standard deviation of the measure. This is explained by the behavior change of the instabilities, the plugs are associated with larger fluctuations that reduce in the transition to superficial waves and stop completely in the fixed bed. It is also possible to observe that higher fluid velocity is related to a higher expansion of the bed, until a fixed condition is reached and its effect on the height is less significant.

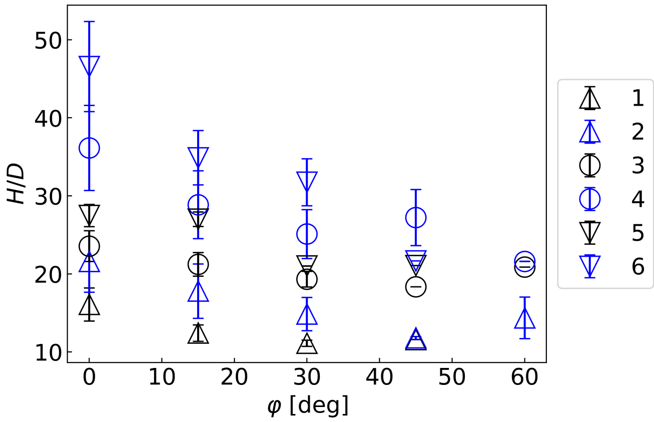

Figure 4.4 – Time-averaged bed height H as function of the inclination angle φ, each symbol represents a different total mass of particles and the blue color indicates a higher cross-sectional mean fluid velocity $\bar{U}$, as seen in the legend that references the cases of the Table 3.1. The error bars correspond to the standard deviation for each run, from Oliveira and Franklin (2024).

The height reduction with inclination also happens in bidisperse micro fluidized beds as seen in Figure 4.5, which shows the average bed height H in function of the inclination angle φ for bidisperse beds, with (a) $0.2\,\mathrm{g}$ and (b) $0.3\,\mathrm{g}$ of glass particles and the error bars represent the standard deviation of the measurement fluctuations. The fluctuations also reduce with inclination in bidisperse beds due to the instabilities transitioning from plugs to waves. It is also noticeable comparing the graphics 4.5a and 4.5b that the greater mass of glass particles reduces the influence of tilting the bed on its expansion.

Figures 4.6a and 4.6b show the average granular temperature across the bed $\langle\theta\rangle$ as a function of the inclination angle φ for mono and bidisperse beds. The plots show an average on time and across the entire bed of the granular temperature, which indicates that the agitation of grains decrease with inclination for the same reason that the bed height reduces. The higher granular temperature occurs in bubble regions in vertical beds, these regions size reduces in the transition to the superficial wave regime, in which the higher temperature is in the superficial movement, and disappear when the condition of fixed bed is reached and grain motion stops.

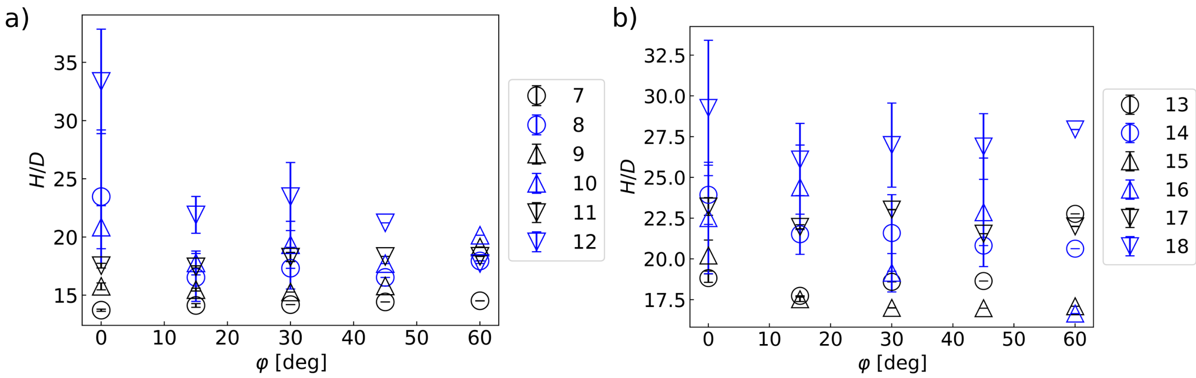

Figure 4.5 – Time-averaged bed height H as function of the inclination angle φ, each symbol represents a different total mass of zirconium particles, with (a) $0.2\,\mathrm{g}$ and (b) $0.3\,\mathrm{g}$ of glass particles and the blue color indicates a higher cross-sectional mean fluid velocity $\bar{U}$, as seen in the legend that references the cases of the Table 3.1. The error bars correspond to the standard deviation for each run, from Oliveira and Franklin (2024).

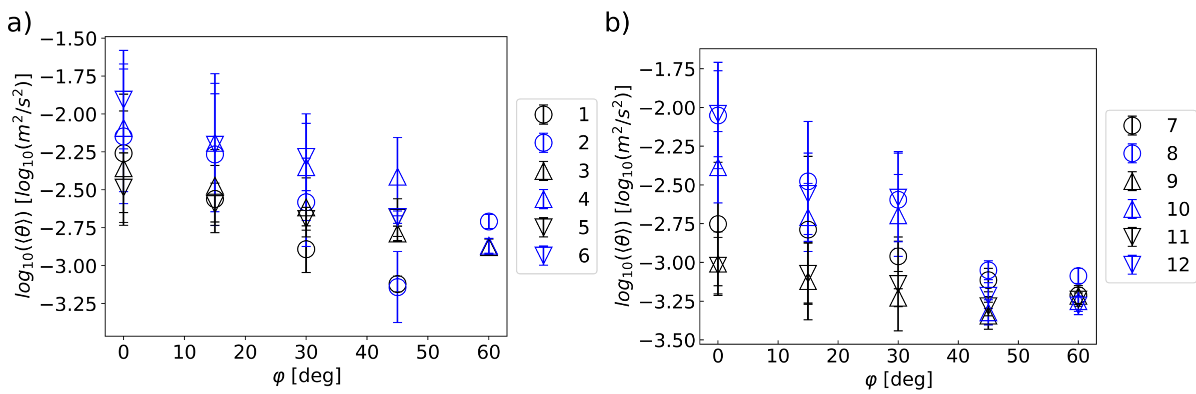

Figure 4.6 – Average granular temperature $\langle\theta\rangle$ calculated in time and across the entire bed in function of the inclination angle φ for (a) monodisperse and (b) bidisperse beds. Equal symbols represent the same total mass of particles and the blue color represents a higher fluid velocity $\bar{U}$, as described in the legend that follows the Table 3.1. The error bars correspond to the standard deviation of measurements, from Oliveira and Franklin (2024).

4.3 Plug length and celerity

Following the measurement procedure described in the previous chapter, the plugs observed in monodisperse cases are grouped in the graphics presented in Figure 4.7. First it is important to note that the case 5 do not produce plugs at inclination of 30° and is not present in the graphics. The graphic 4.7a displays the distribution of plug length λ normalized by the tube diameter D, it shows that inclination has little effect on the average dimensionless plug length, below the natural variation of the measure presented in the box plot. Figure 4.7b present a similar behavior for plug celerity C normalized by cross-sectional mean velocity $\bar{U}$, that its average is also not affected by bed inclination. The first significant influence of inclination is that plugs are not produced by fluidization on highly inclined beds that present surface waves as explained in the previous section. Furthermore, the other noticeable change is the larger spread of plug length in more inclined cases, which is related to the transition of the instabilities to superficial waves.

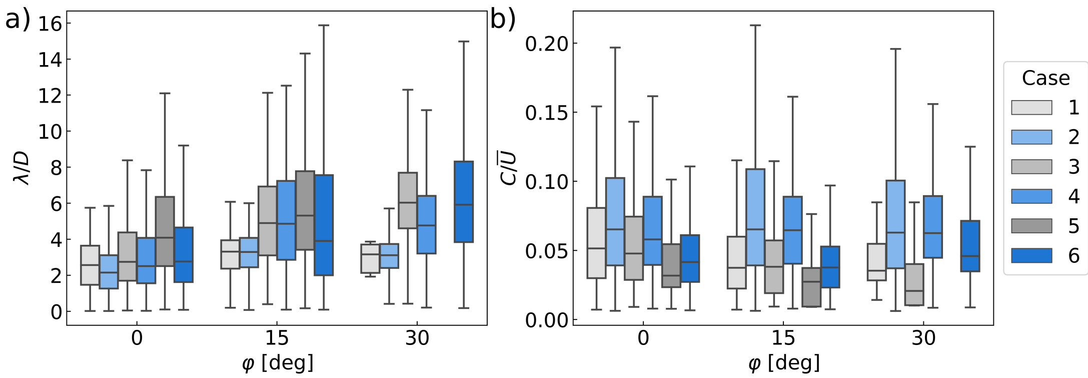

Figure 4.7 – Box plot of the (a) plug length λ and (b) celerity C for each inclination φ where each color represents a case as described in the legend from Table 3.1. The blue color indicates higher $\bar{U}$ compared to the gray bar on left with the same total particle mass. The measures are normalized by the tube diameter D and cross-sectional mean velocity $\bar{U}$ and the maximum angle is 30° because for higher inclinations plugs are not present. Also, the box plot is used to present the distribution of the quantities, from Oliveira and Franklin (2024).

The same analysis is repeated for the plugs in bidisperse micro fluidized beds which yields similar results. Figure 4.8a shows that inclination does not affect the mean length of the plugs beyond the natural variation of plugs observed in the experiments and Figure 4.8b reveals a similar behavior for the celerity of the bidisperse cases compared with monodisperse fluidization. But it is noticeable the larger spread of plug size for higher inclinations as in the previous cases, which is also related to the regime transition discussed previously.

4.4 Circulation of particles in inclined micro fluidized beds

The average motion of particles inside the bed is investigated with the area flux $\vec{A}$ as described in the methodology. Figure 4.9 shows the time average of this measure projected on the frontal plane of the bed for a monodisperse bed and increasing inclinations (case 3 in Table 3.1). The first key observation is that in Figure 4.9a, that portraits a vertical bed, only vertical motion is seen, which is expected from the alignment of the bed axis with the gravity direction. And also because the narrow fluidized beds studied in the group (Cúñez; Franklin,

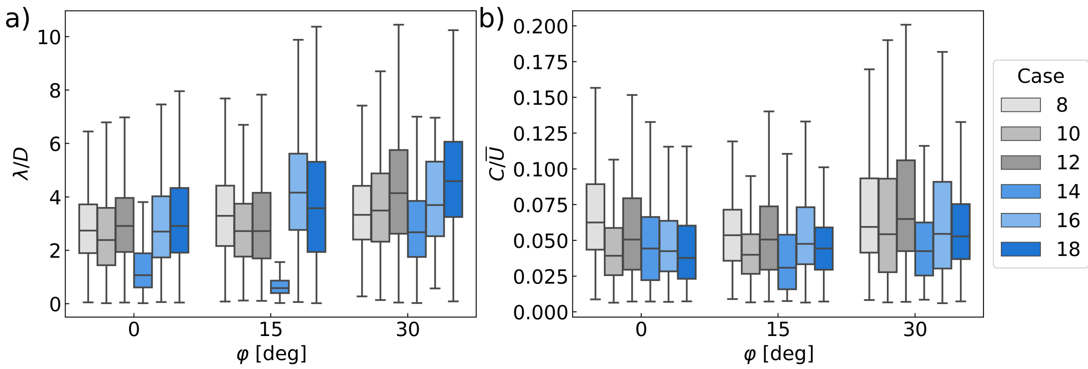

Figure 4.8 – Box plot of the (a) plug length λ and (b) celerity C for each inclination φ where each color represents a case as described in the legend from Table 3.1. The blue color indicates higher $\bar{U}$ compared to the gray bar on left with the same total particle mass. The measures are normalized by the tube diameter D and cross-sectional mean velocity $\bar{U}$ and the maximum angle is 30° because for higher inclinations plugs are not present, also the box plot is used to present the distribution of the quantities, from Oliveira and Franklin (2024).

2019; Cúñez; Franklin, 2020b) do not show the formation of circulation patterns due to strong particle wall interaction.

For the inclinations of 45° and 60° in Figures 4.9d-e there is no movement other than the settling of particles, which is expected for the fixed bed observed in these experiments. The interesting new behavior is observed in intermediate angles of 15° and 30° in Figures 4.9b-c, that show circulation of particles in the bed caused by the misalignment of the tube axis and the gravity direction. In these experiments, the particles on average move upwards in the top surface until they reach the top of the bed and descent in the bottom side.

Figure 4.10 also presents the area flux $\vec{A}$ for different angles of inclination φ but for a higher fluid velocity compared to the previous plots (case 4 in Table 3.1). This shows again only vertical motion in the vertically aligned bed of Figure 4.10a and fixed bed with only settling particles that cause the isolated flux measures seen in Figures 4.10d-e for the inclination angles of $\varphi = 45°$ and 60°. In the intermediate angles of $\varphi = 15°$ and 30°, the circulation can be noticed like in the previous case, but it is stronger as indicated by the larger arrows (the scale is the same in all plots). That suggests that higher fluid velocity leads to higher local flux of particles (with higher velocity, there is little variation in the packing fraction) and stronger average circulation.

For bidisperse bed, Figure 4.11 shows that circulation is still present on intermediate inclination angles. It is possible to observe in Figure 4.11a that only vertical motion is present on vertically aligned beds. And in Figure 4.11e that in a fixed bed only the settling motion of

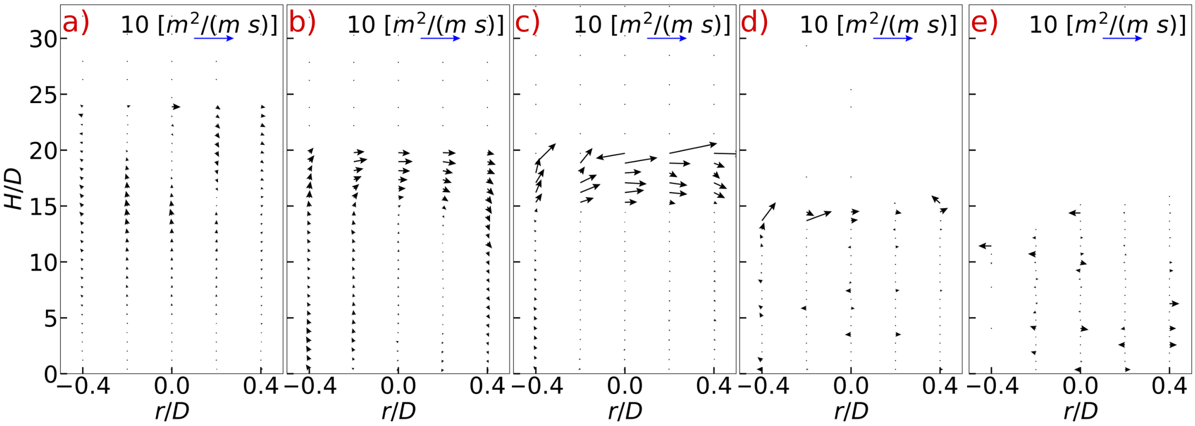

Figure 4.9 – Vector plot of the average area flux $\vec{A}$ projected in the frontal plane of the tube, described by height and radius normalized by the diameter, of a monodisperse bed with $0.5\,\mathrm{g}$ of glass particles and $\bar{U} = 1.57\,\mathrm{m\,s^{-1}}$. Each vector represents the particle flux in a cell and the scale is presented in blue. The plots represent the case 3 of Table 3.1 (monodisperse bed) with the different inclinations: φ = (a) 0°, (a) 15°, (a) 30°, (a) 45° and (a) 60°. The blue arrow is the scale for each plot. Reproduced from Oliveira and Franklin (2024).

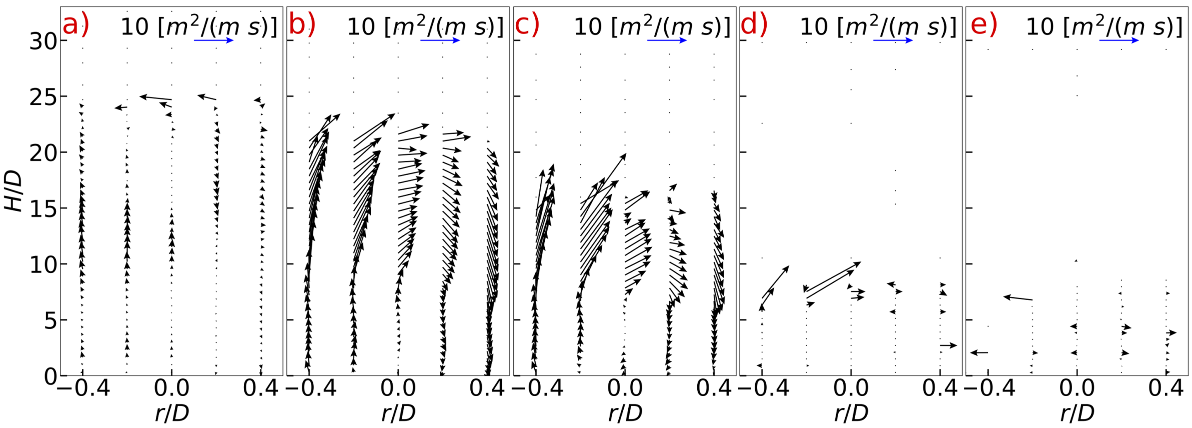

Figure 4.10 – Vector plot of the average area flux $\vec{A}$ projected in the frontal plane of the tube, described by height and radius normalized by the diameter, of a monodisperse bed with $0.5\,\mathrm{g}$ of glass particles and $\bar{U} = 1.77\,\mathrm{m\,s^{-1}}$. Each vector represents the particle flux in a cell and the scale is presented in blue. The plots represent the case 4 of Table 3.1 (monodisperse bed) with the different inclinations: φ = (a) 0°, (a) 15°, (a) 30°, (a) 45° and (a) 60°. The blue arrow is the scale for each plot. Reproduced from Oliveira and Franklin (2024).

particles to form an air channel is present. In this specific experiment the settling process was longer than usual, and it shows up in the plot, when in other cases it is contained entirely in the start time that is not considered in the time averages and do not appear on the plots.

On the intermediate inclinations $\varphi = 15°$ to 45° in Figures 4.11b-d the circulation pattern can be seen in the top of the bed (above the dimensionless height of 5) but it is not present in the bottom. This happens because the bottom layer is not completely fluidized in this condition, which reduces the particles' mobility and by consequence their flux and the circulation. Nevertheless, it is clear that the circulation is still present in bidisperse beds and it may lead to mixing in the bed, as proposed by Hudson *et al.* (1996), which will be investigated in the next section.

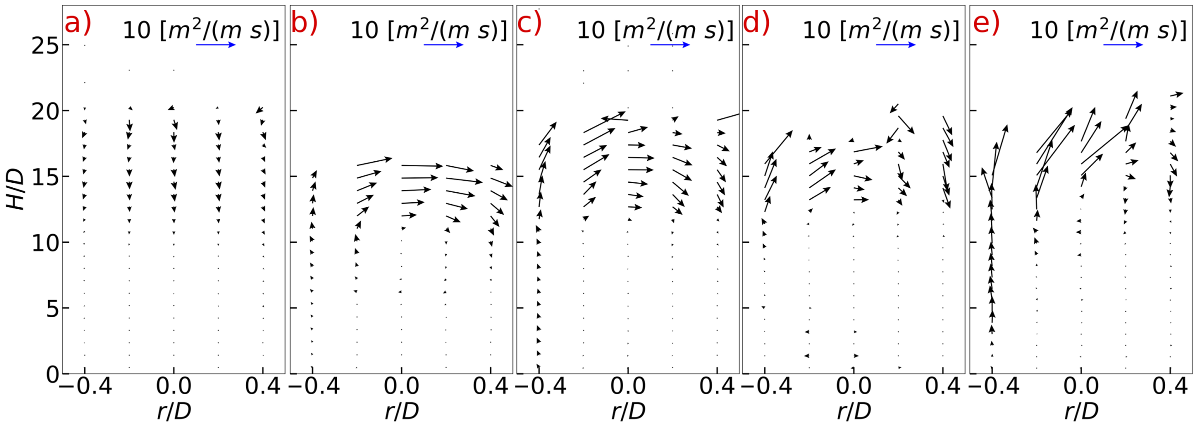

Figure 4.11 – Vector plot of the average area flux $\vec{A}$ projected in the frontal plane of the tube, described by height and radius normalized by the diameter, of a bidisperse bed with $0.3\,\mathrm{g}$ of glass and $0.5\,\mathrm{g}$ of zirconium particles and $\bar{U} = 1.77\,\mathrm{m\,s^{-1}}$. Each vector represents the particle flux in a cell and the scale is presented in blue. The plots represent the case 16 of Table 3.1 (bidisperse bed) with the different inclinations: $\varphi =$ (a) 0°, (a) 15°, (a) 30°, (a) 45° and (a) 60°. The blue arrow is the scale for each plot. Reproduced from Oliveira and Franklin (2024).

In Figure 4.12 the time window is reduced to $0.1\,\mathrm{s}$ to investigate the mechanism of the average circulation, also the packing fraction is displayed with the colors indicated in the legend. It is possible to see that the circulation is confined to the bubble regions and move with them upwards in the bed. The combination of the rotation inside the bubbles and the upwards motion averages in time to the global circulation show previously. But the fact that the circulation occurs in small regions is an important difference from the average behavior because it means no particle is transported through the entire bed height in a single motion, the overall effect is closer to mixing in a small length scale.

In conclusion, the non-monotonic behavior of the circulation of particles inside the bed can be observed in Figure 4.13 for (a) mono- and (b) bidisperse beds, with a maximum in intermediate angles $15° \leq \varphi \leq 45°$ as seen in the vector plots. The negative values on the graphics are due to the direction of rotation being opposite to the z-axis direction. It is possible to see that higher fluid velocity, indicated by the blue color of the symbols, leads to a

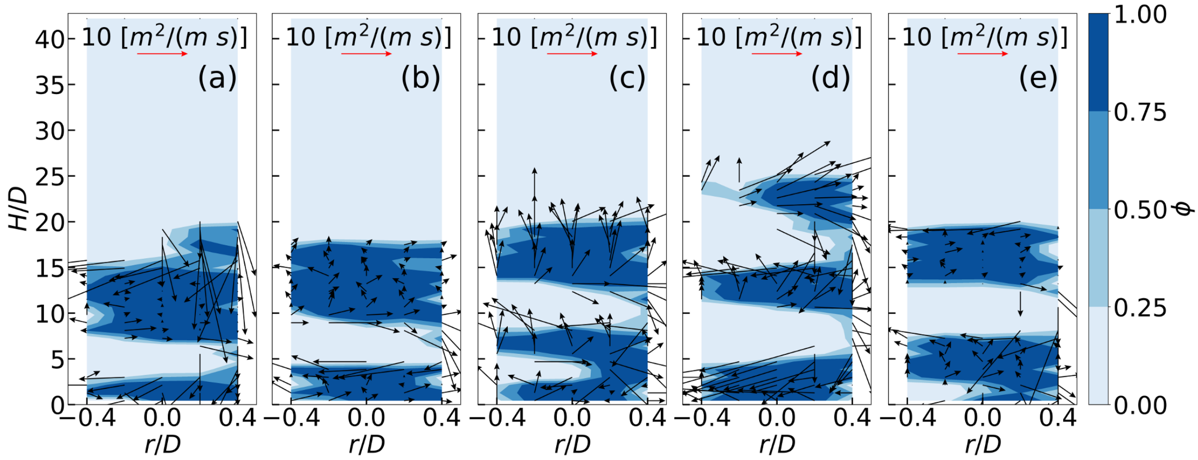

Figure 4.12 – Vector plot of the average area flux $\vec{A}$ projected in the frontal plane of the tube, described by height and radius normalized by the diameter, of a monodisperse bed with $0.5\,\mathrm{g}$ of glass particles and $\bar{U} = 1.77\,\mathrm{m\,s^{-1}}$, the vectors are superimposed to the packing fraction ϕ. Each vector represents the particle flux in a cell, the scale is presented in red and the colors correspond to the packing fraction whose values are available in the legend. The plots represent the case 4 of Table 3.1 for 5 different instants: (a) t_0, (b) $t_0 + 0.1\,\mathrm{s}$, (c) $t_0 + 0.2\,\mathrm{s}$, (d) $t_0 + 0.3\,\mathrm{s}$ and (e) $t_0 + 0.4\,\mathrm{s}$. The red arrow is the scale for each plot. Reproduced from Oliveira and Franklin (2024).

more intense circular motion of the solids, this is an interesting observation that can be used to explain the mixing observed in the following section.

4.5 Mixing in bidisperse beds

An interesting result about inclined micro fluidized beds discussed previously is the formation of a mixing layer, as described in the methodology a mixing measurement is developed to represent properly the conditions observed in the experiments. Figure 4.14 shows the mixing layer size M relative to the bed as a function of the inclination angle φ for different masses of particles in the bed and fluid velocities. It is possible to observe that larger fluid velocity, represented by the blue color, leads to a higher degree of mixing, which is expected as the larger fluidization velocity causes the bed to be more agitated.

Another interesting result seen in Figures 4.14a and 4.14b is that there is a maximum for the mixing between the angles of 30° to 45°. This is the result of the competition between the circulation that increases with the inclination and the worse fluidization at higher inclinations that decreases particle mobility and prevents the circulation and mixing. To better emphasize this link, the mixture layer M is plotted against the dimensionless bed moment L (normalized

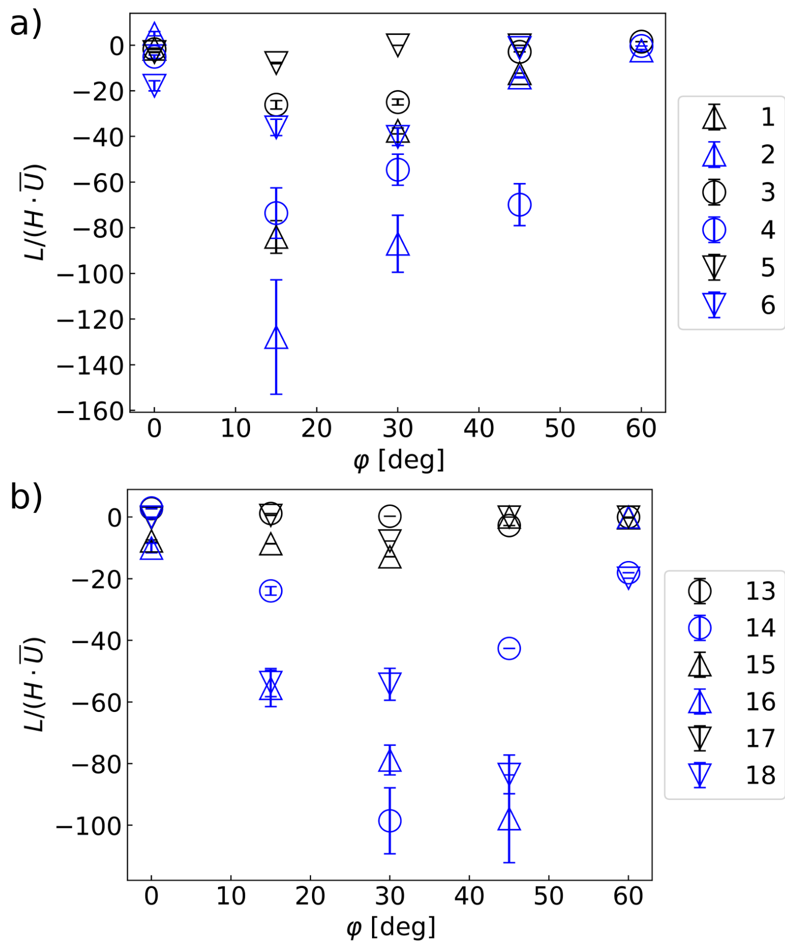

Figure 4.13 – Bed moment L that indicates circulation as described in the methodology for the (a) monodisperse and (b) bidisperse bed. Each point represents a case in Table 3.1 as per the legend, the color blue indicates higher fluid velocity $\bar{U}$ and the error bars correspond to the standard deviation of the measurements. Reproduced from Oliveira and Franklin (2024).

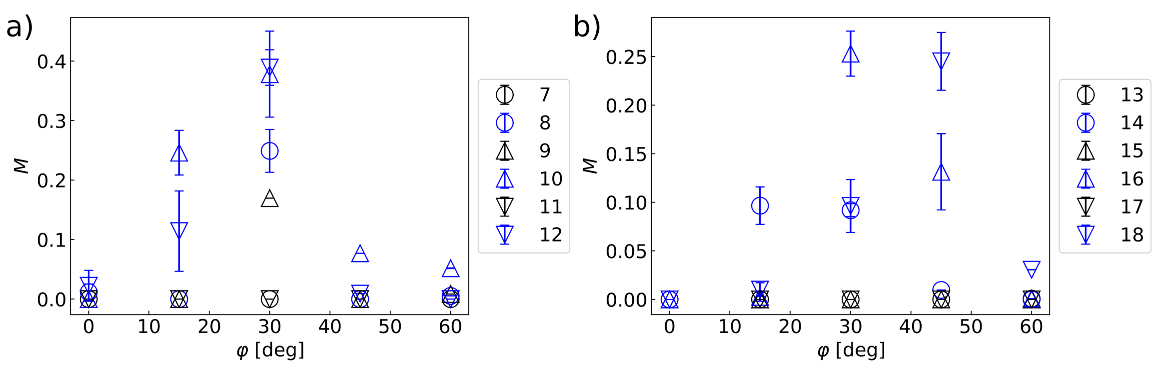

Figure 4.14 – Size of mixing layer M measured with regions as described in the methodology for bed with (a) $0.2\,\mathrm{g}$ and (b) $0.3\,\mathrm{g}$ of glass particles. Each point represents a case in Table 3.1 as per the legend, the color blue indicates higher fluid velocity $\bar{U}$ and the error bars correspond to the standard deviation of the measurements. Reproduced from Oliveira and Franklin (2024).

by H and $\bar{U}$), which is a measure of circulation in the bed, in Figure 4.15.

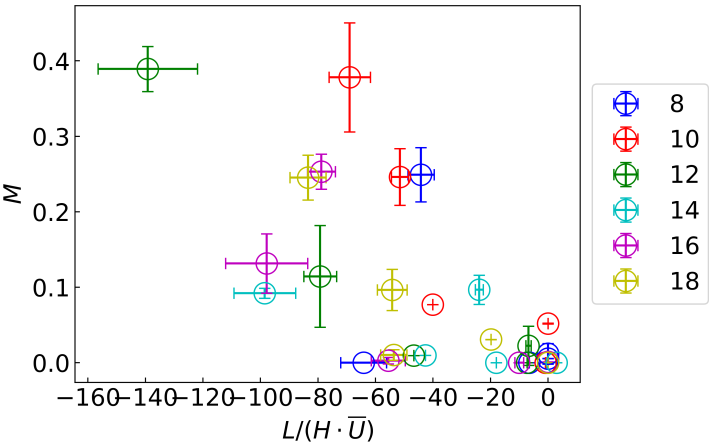

Figure 4.15 – Relation between the normalized bed moment L and the mixing layer size M. Each color represent a case described in the legend that follows the Table 3.1 and the error bars correspond to the standard deviation of the measurements. Reproduced from Oliveira and Franklin (2024).

This direct comparison between circulation and mixing in Figure 4.15 uses only the cases in Table 3.1 with higher fluid velocity to avoid accumulating points in the bottom right, with low mixing and moment. It is possible to see a direct relation between the measurements, with higher bed moment in modulus associated with a higher mixing degree. It is also important to notice the points with higher bed moment but no mixing, this can be explained by circulation contained entirely in the top layer of particles. Which is caused by a bottom layer in a fixed bed condition due to insufficient fluid velocity. This prevents mixing because the particles in the fixed bed are not mobile and can not mix with the top layer.

4.6 Preliminary results of numerical simulations

The first result is the comparison of bed height H as a function of time to verify the improvements to the model. In the Figure 4.16 it is possible to see a better agreement between the curves than the previous results shown in Figure 3.11 in a bed with $0.3\,\mathrm{g}$ of glass particles and superficial velocity of $1.77\,\mathrm{m\,s^{-1}}$. The error in average bed height was reduced from close to 100% to about 50% in the vertical case and from 60% to 40% in the bed with 15° of inclination.

Using the particle data, an interesting visualization is the average particle velocity in different sections of the bed. Figure 4.17 shows the three velocity components (u, v and w) in the cross-section of the tube averaged both in time and in the axial direction in the height

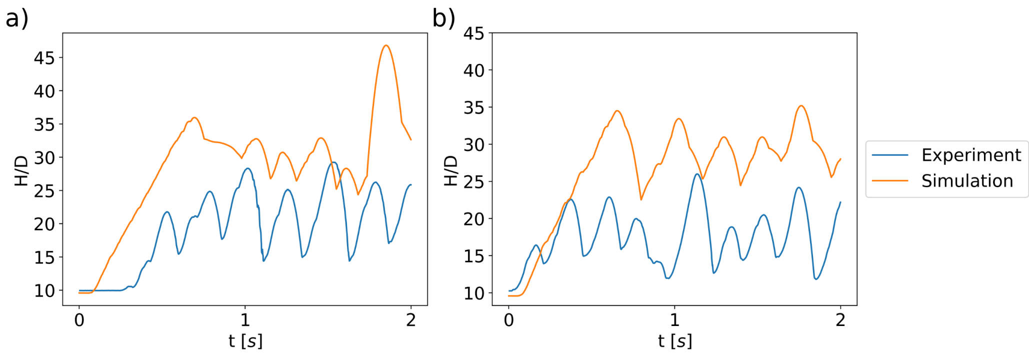

Figure 4.16 – Comparison of bed height H in the experiments and numerical simulations showing the discrepancy of the results and the incompatibility between model and experimental results with $0.3\,\mathrm{g}$ of glass particles, $\bar{U} = 1.77\,\mathrm{m\,s^{-1}}$ and inclination of $\varphi =$ (a) $0°$ and (b) $15°$

range from 10 to $12\,\mathrm{cm}$ for a vertical bed. And, for comparison, Figure 4.18 presents the same cross-sectional profile in the bottom of the bed, from height 0 to $2\,\mathrm{cm}$. In the vertical bed there is little difference in the regions and due to wall effects, on average the particles climb faster in the center. And, it is important to notice that the axial component is an order of magnitude larger than the others, which is expected because this is the main direction of motion in the bed.

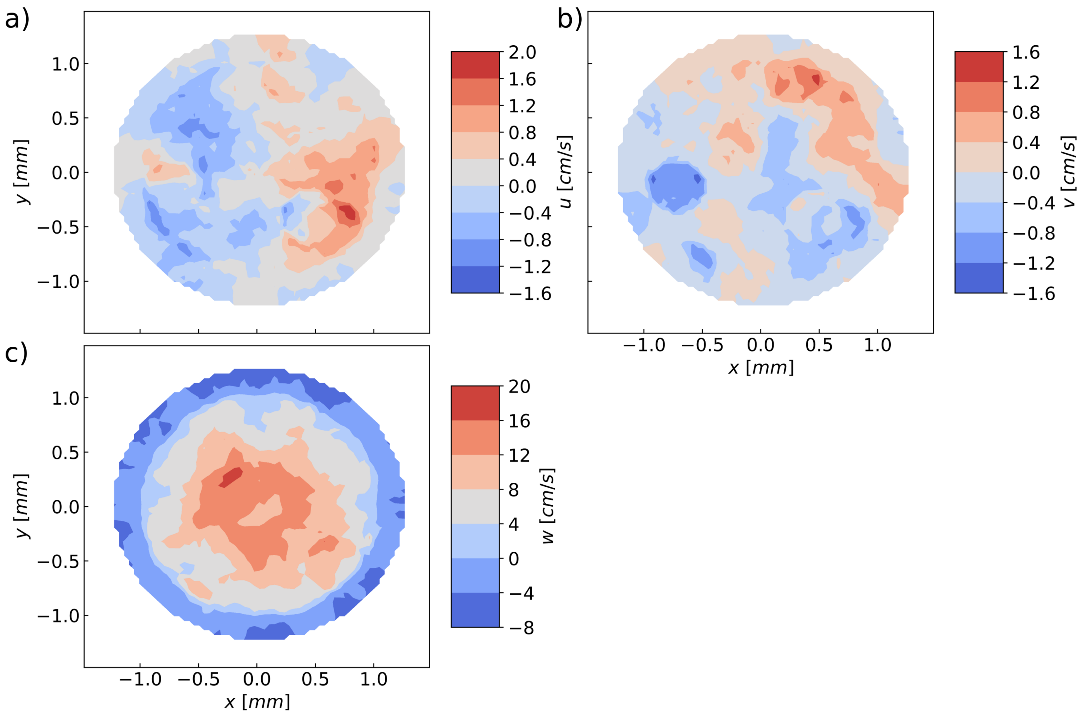

Figure 4.17 – Average velocity of the solids in the tube section from 10 to $12\,\mathrm{cm}$ presented as cross-sectional field and with the (a) u, (b) v and (c) w components divided in each graphic, from the simulation with $0.3\,\mathrm{g}$ of glass particles, $\bar{U} = 1.77\,\mathrm{m\,s^{-1}}$ and inclination $\varphi = 0°$.

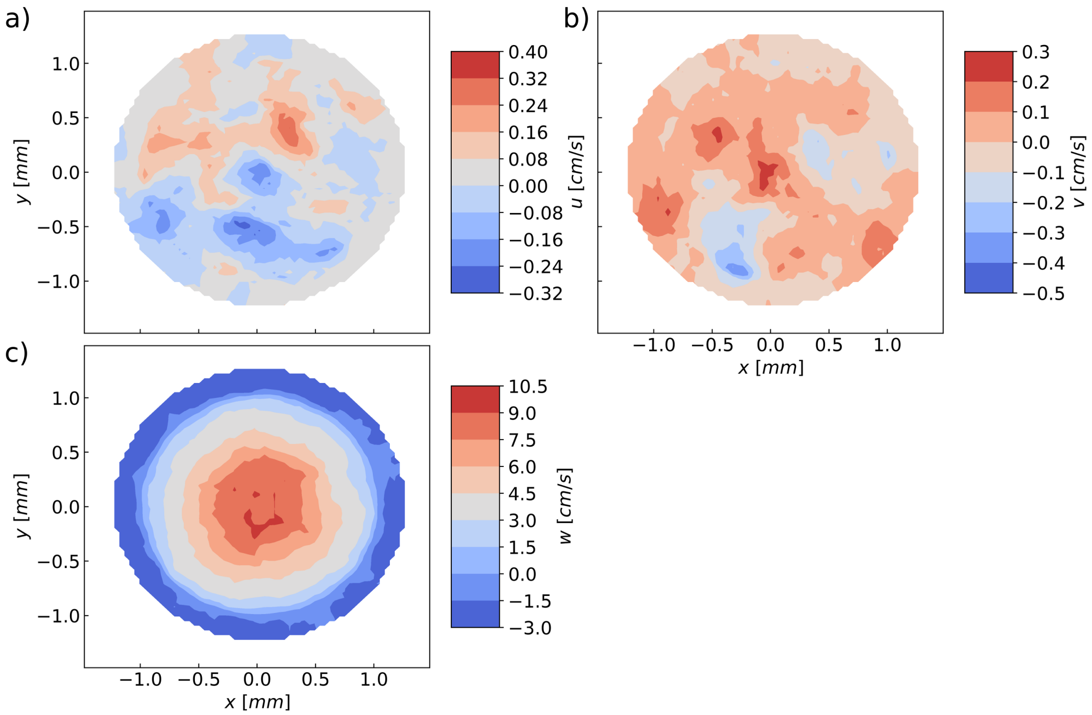

Figure 4.18 – Average velocity of the solids in the tube section from 0 to $2\,\mathrm{cm}$ presented as cross-sectional field and with the (a) u, (b) v and (c) w components divided in each graphic, from the simulation with $0.3\,\mathrm{g}$ of glass particles, $\bar{U} = 1.77\,\mathrm{m\,s^{-1}}$ and inclination $\varphi = 0°$.

By doing the same analysis in a bed inclined $15°$ with respect to the gravity there is a significant change in the velocity profiles, seen in Figures 4.19 e 4.20 for the top $(10{-}12\,\mathrm{cm})$ and bottom $(0{-}2\,\mathrm{cm})$ of the bed respectively. The inclination is a clockwise rotation in the x direction, therefore more positive y values are at the bottom of the bed, which means there is a component of the gravity acceleration towards the positive direction in the y-axis. The first important difference is in the axial component w that shows an average upwards motion in the top of the bed (negative y values) and downwards in the bottom of the bed (positive y values). Furthermore, in the top section the solids follow the gravity direction with a positive v component and then complete the circulation in the bottom section with a negative v component. Despite the circulation, this component is still an order of magnitude lower than the axial component. In the u component it is possible to see in the top section that the particles go from the center of the tube towards the edges, and it is quite symmetrical, as there is no asymmetry in this direction. Similarly, in the bottom section the particles go from the edges towards the center.

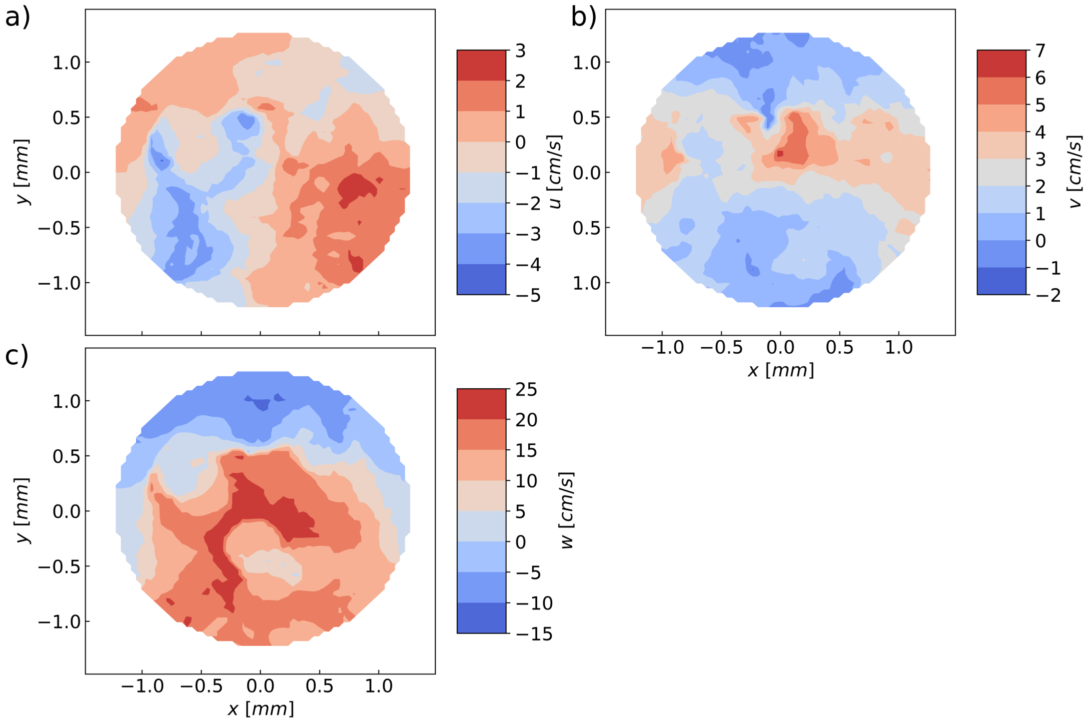

Figure 4.19 – Average velocity of the solids in the tube section from 10 to $12\,\mathrm{cm}$ presented as cross-sectional field and with the (a) u, (b) v and (c) w components divided in each graphic, from the simulation with $0.3\,\mathrm{g}$ of glass particles, $\bar{U} = 1.77\,\mathrm{m\,s^{-1}}$ and inclination $\varphi = 15°$.

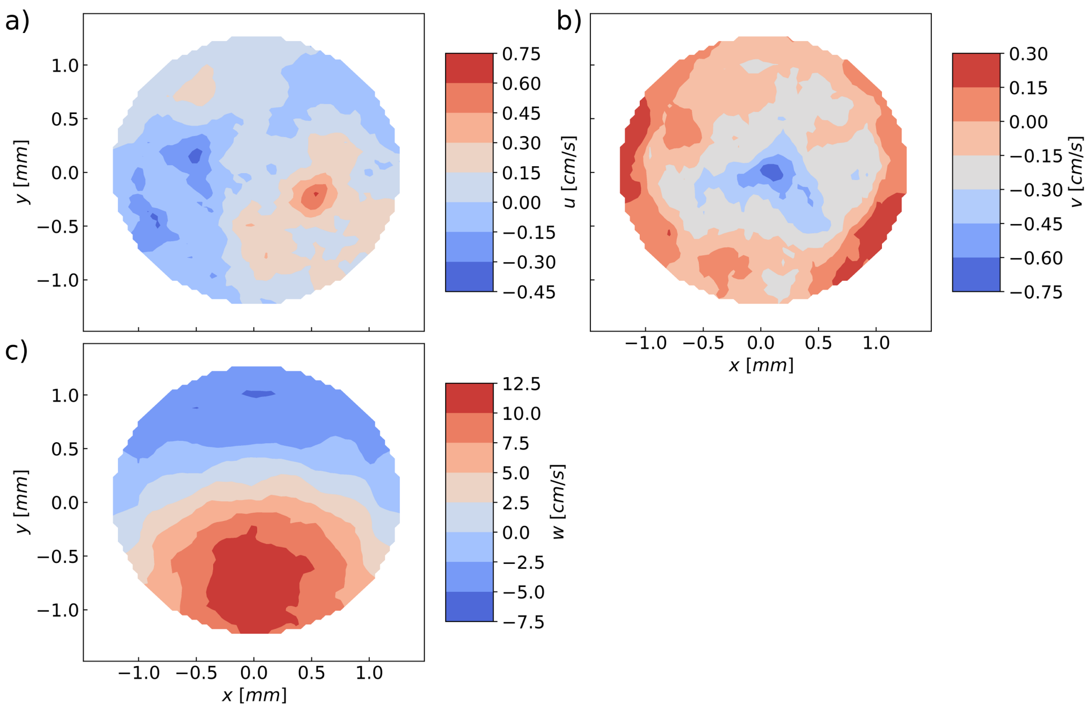

Figure 4.20 – Average velocity of the solids in the tube section from 0 to $2\,\mathrm{cm}$ presented as cross-sectional field and with the (a) u, (b) v and (c) w components divided in each graphic, from the simulation with $0.3\,\mathrm{g}$ of glass particles, $\bar{U} = 1.77\,\mathrm{m\,s^{-1}}$ and inclination $\varphi = 15°$.

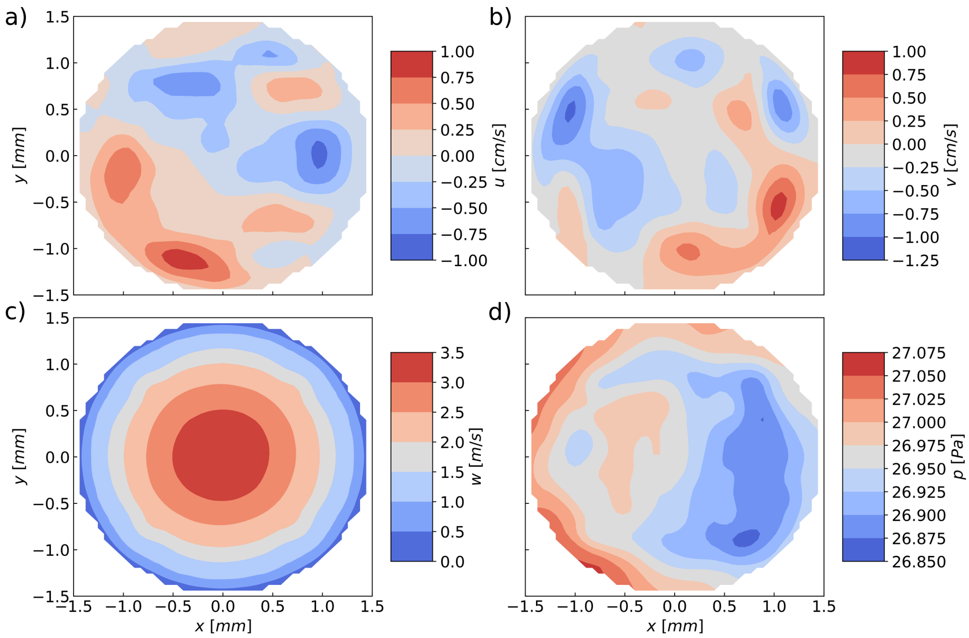

Figure 4.21 – Average velocity of the fluid in the tube section from 10 to $12\,\mathrm{cm}$ presented as cross-sectional field and with the (a) u, (b) v and (c) w components divided in each graphic. There is also (d) the average manometric pressure field of the fluid in the section, from the simulation with $0.3\,\mathrm{g}$ of glass particles, $\bar{U} = 1.77\,\mathrm{m\,s^{-1}}$ and inclination $\varphi = 0°$.

The fluid velocity profile is analyzed in the same way as the solids velocity profile presented previously with an addition of the pressure field. In Figures 4.21 and 4.22 the fields are presented for the simulations of $0.3\,\mathrm{g}$ of glass particles, $\bar{U} = 1.77\,\mathrm{m\,s^{-1}}$ in a vertical tube, it is possible to see that the axial velocity is much higher than the average solid velocity, but the fluctuations in the cross-sectional plane have similar magnitudes. Also, the pressure drop in the bed is small and is very uniform across the plane. Interestingly, the v and w fields are more symmetrical in bottom section, but only the axial velocity profile matches with the solid's profile in Figure 4.19, this indicates that the cross-sectional motion is mainly fluctuations that do not affect the general fluidization behavior.

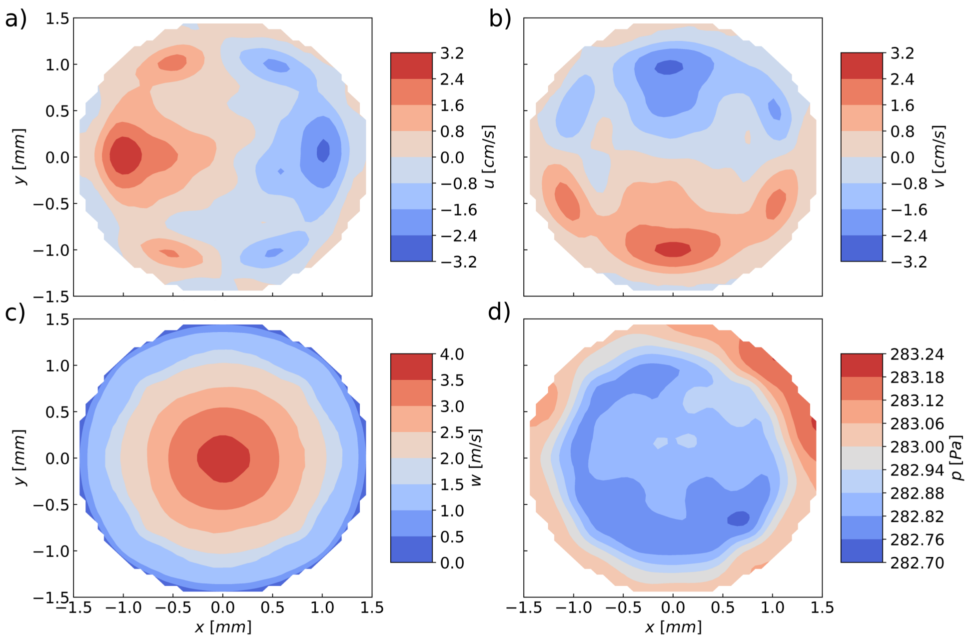

Figure 4.22 – Average velocity of the fluid in the tube section from 0 to $2\,\mathrm{cm}$ presented as cross-sectional field and with the (a) u, (b) v and (c) w components divided in each graphic. There is also (d) the average manometric pressure field of the fluid in the section, from the simulation with $0.3\,\mathrm{g}$ of glass particles, $\bar{U} = 1.77\,\mathrm{m\,s^{-1}}$ and inclination $\varphi = 0°$.

In Figures 4.23 and 4.24 the top and bottom sections are presented respectively, with the same simulation conditions and an inclination of $\varphi = 15°$. It is possible to see the same general conclusions of the previous results: a higher axial average velocity, low pressure drop and uniform pressure field. It is possible to see in the w component that the zone of higher fluid velocity is displaced towards the top of the tube (y-axis negative values), and the average circulation with positive v component in the top section and negative v component in the bottom. The u component is symmetrical as the solid's velocity and has a similar profile of flow from the edges towards the center. The pressure field in the bottom is also slightly displaced, with higher pressure in the bottom of the bed, where there are more particles.

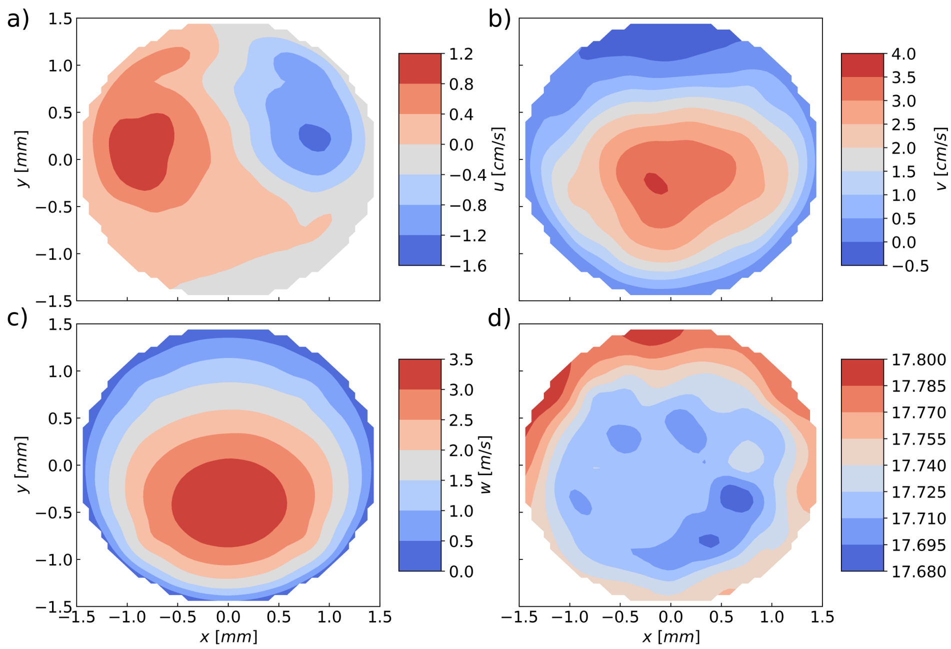

Figure 4.23 – Average velocity of the fluid in the tube section from 10 to $12\,\mathrm{cm}$ presented as cross-sectional field and with the (a) u, (b) v and (c) w components divided in each graphic. There is also (d) the average manometric pressure field of the fluid in the section, from the simulation with $0.3\,\mathrm{g}$ of glass particles, $\bar{U} = 1.77\,\mathrm{m\,s^{-1}}$ and inclination $\varphi = 15°$.

The particles and fluid velocity profiles presented in Figure 4.17 to 4.24 show that the fluid and solids have resembling profiles, moving with similar profiles which shows that the two phases are coupled up to a certain point.

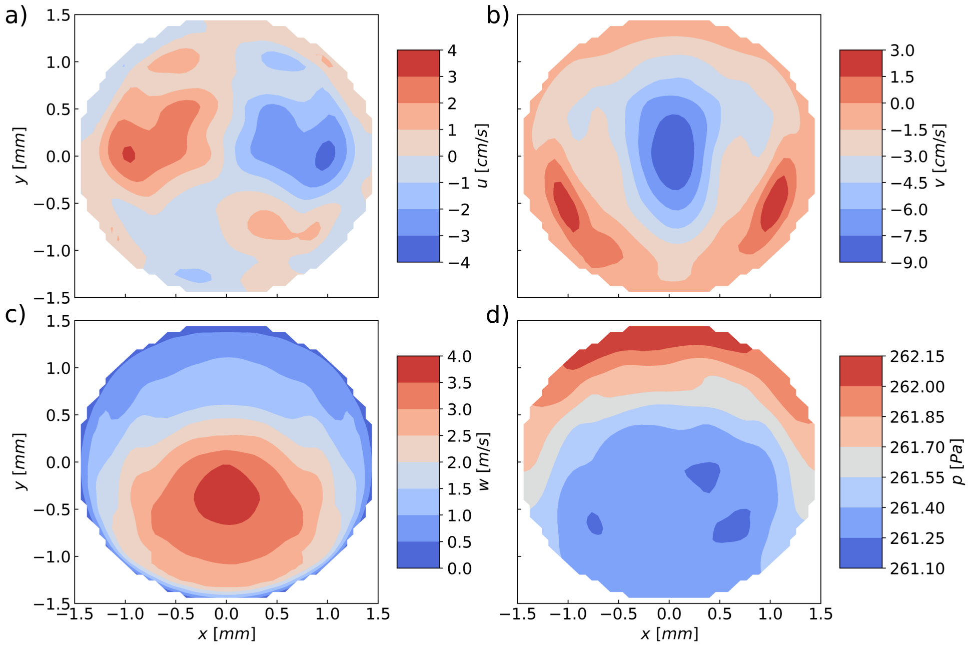

Figure 4.24 – Average velocity of the fluid in the tube section from 0 to $2\,\mathrm{cm}$ presented as cross-sectional field and with the (a) u, (b) v and (c) w components divided in each graphic. There is also (d) the average manometric pressure field of the fluid in the section, from the simulation with $0.3\,\mathrm{g}$ of glass particles, $\bar{U} = 1.77\,\mathrm{m\,s^{-1}}$ and inclination $\varphi = 15°$.

5 CONCLUSION

5.1 Conclusions

In this MSc Thesis, the behavior of gas-solid micro fluidized beds is investigated, with both mono- and bidisperse beds under different inclinations. The glass and zirconium particles used in the experiments have diameters close to the tube, characterizing a very-narrow fluidized bed ($D/d \approx 6$) that presents strong confinement effects. The experiments were filmed with a high-speed camera and the images processed to acquire measurements at grain and bed scale, which allowed for a better understanding of the individual particle motion and how it affects the fluidized bed behavior.

In the monodisperse beds, it is observed that the plug-like instabilities present in vertical beds gradually change into superficial waves as the bed is tilted, with no plugs observed with an inclination angle φ higher than 30°. For shallow angles of inclination ($0° \leq \varphi \leq 30°$), the plugs' average length and celerity remain roughly constant for all angles tested. A similar behavior is also observed in bidisperse beds. Both types of bed also present a reduction in granular temperature as the inclination angle increases, which is an indication of worse fluidization in this condition.

Inclined micro fluidized beds promote mixing of particles in bidisperses case, which may be useful in applications that require mixing of different types of particles. In this work, the experiments using two types of particles with different densities show that tilting the fluidized bed changes the segregation regime, due to kinetic sieving in vertical beds, to the formation of a mixing layer in moderate inclinations, and ultimately forming an air channel in the top of a fixed bed for higher inclination angles.

It is observed that the mixing degree changes non-monotonically with inclination, with a maximum in an angle in the range $30° \leq \varphi \leq 45°$ that depends on the mass of particles in the bed and the fluidization velocity. The minima, when no mixing is observed, occur in the vertical case ($\varphi = 0°$) and for larger inclinations $\varphi \geq 45°$ that correspond to the segregating regime and a fixed bed condition respectively.

The circulation of particles represented by the normalized bed moment follows the same pattern of mixing, a maximum in the range of $30° \leq \varphi \leq 45°$ and no circulation is observed in vertical beds and above 45°. This is an indication that the formation of the mixing layer occurs as a competition between circulation promoted by the fluid flow and the kinetic sieving. This direct relationship can be observed in the diagram comparing the mixing index M and the normalized bed moment L for the cases used in this study. Furthermore, diagrams of mixing M as a function of the inclination angle φ can be used as a guide to achieve better mixing in industrial applications.

As for the numerical simulations, the simplifications in the models used were unable to represent all details of fluidization and some errors are observed with in comparison with the experiments. Nevertheless, there is a good representation of the phenomena observed that can be used for qualitative analysis, such as the average velocity profiles of solids and fluid that provide insights on how the two phases movement resemble each other.

The velocity profiles of solids and fluid are similar, which indicates the link between the two phases in the micro fluidized bed. Despite the resemblance, the magnitude of the fluid velocity is approximately 10 times higher than the magnitude of the solids' velocity. It is also noticeable that the axial component is at least two orders of magnitude larger than the transversal components due to the narrow profile of the bed that favors greatly this direction of motion.

5.2 Future works

For future works, it would be interesting to extend the investigation about mixing in inclined micro fluidized beds conducted for two types of particles with different densities, as to investigate the size segregation and shape segregation. It is known that in vertical fluidized beds size segregation occurs, similarly to the density segregation explored in this work, therefore an investigation into the changes promoted by an inclination of the bed and comparison with the density segregation would improve the knowledge of micro fluidized beds.

It would also be interesting to continue the investigation on numerical models of micro fluidized beds, with the development of new drag correlations more appropriate to this case. And also new simulation methods using resolved immersed boundary models to tackle the limitations of the method, such as the need to use drag correlations or perform the costly resolved method for the boundaries of the particles. Another necessary development is new numerical models for static electric charging due to collisions, as it is a relevant effect that changes the behavior of micro fluidized beds introducing electrical charges in the particles and tube wall.

BIBLIOGRAPHY

Agrawal, V.; Shinde, Y.; Shah, M. T.; Utikar, R. P.; Pareek, V. K.; Joshi, J. B. Effect of drag models on CFD–DEM predictions of bubbling fluidized beds with Geldart D particles. **Advanced Powder Technology**, v. 29, n. 11, p. 2658–2669, nov. 2018.

Ahrens, J.; Geveci, B.; Law, C. ParaView: An End-User Tool for Large Data Visualization. In: Hansen, C. D.; Johnson, C. R. (Ed.). **The Visualization Handbook**. Amsterdam ; Boston: Elsevier-Butterworth Heinemann, 2005. ISBN 978-0-12-387582-2.

Amorij, J. P.; Huckriede, A.; Wilschut, J.; Frijlink, H. W.; Hinrichs, W. L. J. Development of Stable Influenza Vaccine Powder Formulations: Challenges and Possibilities. **Pharm. Res.**, v. 25, p. 1256–1273, 2008.

Anderson, T. B.; Jackson, R. Fluid Mechanical Description of Fluidized Beds. Stability of State of Uniform Fluidization. **Industrial & Engineering Chemistry Fundamentals**, v. 7, n. 1, p. 12–21, fev. 1968.

Azad, M. A.; Osorio, J. G.; Brancazio, D.; Hammersmith, G.; Klee, D. M.; Rapp, K.; Myerson, A. A compact, portable, re-configurable, and automated system for on-demand pharmaceutical tablet manufacturing. **Internat. J. Pharmaceut.**, v. 539, n. 1, p. 157–164, 2018.

Azad, M. A.; Osorio, J. G.; Wang, A.; Klee, D. M.; Eccles, M. E.; Grela, E.; Sloan, R.; Hammersmith, G.; Rapp, K.; Brancazio, D.; Myerson, A. S. On-Demand Manufacturing of Direct Compressible Tablets: Can Formulation Be Simplified? **Pharm Res**, v. 36, p. 167, 2019.

Bello, M. M.; Abdul Raman, A. A.; Purushothaman, M. Applications of fluidized bed reactors in wastewater treatment – A review of the major design and operational parameters. **Journal of Cleaner Production**, v. 141, p. 1492–1514, jan. 2017.

Bertsekas, D. P. Auction algorithms for network flow problems: A tutorial introduction. **Computational Optimization and Applications**, v. 1, n. 1, p. 7–66, out. 1992.

Boffito, D. C.; Neagoe, C.; Edake, M.; Pastor-Ramirez, B.; Patience, G. S. Biofuel synthesis in a capillary fluidized bed. **Catal. Today**, v. 237, p. 13–17, 2014.

Burns, S. J.; Piiroinen, P. T.; Hanley, K. J. Critical time step for DEM simulations of dynamic systems using a Hertzian contact model. **International Journal for Numerical Methods in Engineering**, v. 119, n. 5, p. 432–451, ago. 2019.

Capece, M.; Dave, R. Application of fluidized bed film coating for membrane encapsulation of catalysts. **Powder Technology**, v. 211, n. 2-3, p. 199–206, ago. 2011.

Carvalho, D. D.; Lima, N. C.; Franklin, E. M. Impact craters formed by spinning granular projectiles. **Physical Review E**, v. 108, n. 5, p. 054904, nov. 2023.

Chaikittisilp, W.; Taenumtrakul, T.; Boonsuwan, P.; Tanthapanichakoon, W.; Charinpanitkul, T. Analysis of solid particle mixing in inclined fluidized beds using DEM simulation. **Chemical Engineering Journal**, v. 122, n. 1, p. 21–29, set. 2006.

Chen, Y.-M. Applications for Fluid Catalytic Cracking. In: **Handbook of Fluidization and Fluid-Particles Systems**. New York: Marcel Dekker, 2003, (Chemical Industries, 91). p. 379–396. ISBN 978-0-8247-0259-5.

Cortazar, M.; Lopez, G.; Alvarez, J.; Arregi, A.; Amutio, M.; Bilbao, J.; Olazar, M. Experimental study and modeling of biomass char gasification kinetics in a novel thermogravimetric flow reactor. **Chemical Engineering Journal**, v. 396, p. 125200, set. 2020.

Cúñez, F. D.; Franklin, E. Plug regime in water fluidized beds in very narrow tubes. **Powder Technology**, v. 345, p. 234–246, mar. 2019.

Cúñez, F. D.; Franklin, E. M. Crystallization and jamming in narrow fluidized beds. **Physics of Fluids**, v. 32, n. 8, p. 083303, ago. 2020.

Cúñez, F. D.; Franklin, E. M. Mimicking layer inversion in solid-liquid fluidized beds in narrow tubes. **Powder Technology**, v. 364, p. 994–1008, mar. 2020.

Cúñez, F. D.; Franklin, E. M. Miniaturized gas–solid fluidized beds. **Mechanics Research Communications**, v. 131, p. 104146, ago. 2023.

Cúñez, F. D.; Lima, N. C.; Franklin, E. M. Motion and clustering of bonded particles in narrow solid–liquid fluidized beds. **Phys. Fluids**, v. 33, n. 2, p. 023303, 2021.

Dewettinck, K.; Huyghebaert, A. Fluidized bed coating in food technology. **Trends in Food Science & Technology**, v. 10, n. 4-5, p. 163–168, abr. 1999.

Ding, J.; Gidaspow, D. A bubbling fluidization model using kinetic theory of granular flow. **AIChE Journal**, v. 36, n. 4, p. 523–538, abr. 1990.

Du, B.; Warsito, W.; Fan, L.-S. ECT Studies of Gas-Solid Fluidized Beds of Different Diameters. **Industrial & Engineering Chemistry Research**, v. 44, n. 14, p. 5020–5030, jul. 2005.

El-Emam, M. A.; Zhou, L.; Shi, W.; Han, C.; Bai, L.; Agarwal, R. Theories and Applications of CFD–DEM Coupling Approach for Granular Flow: A Review. **Archives of Computational Methods in Engineering 2021**, v. 1, p. 1–42, abr. 2021.

Ergun, S. Fluid Flow Trough Packed Columns. **Fluid Floww Trough Packed Columns**, v. 48, n. 2, p. 89–94, 1952.

Ervasti, T.; Simonaho, S.-P.; Ketolainen, J.; Forsberg, P.; Fransson, M.; Wikström, H.; Folestad, S.; Lakio, S.; Tajarobi, P.; Abrahmsén-Alami, S. Continuous manufacturing of extended release tablets via powder mixing and direct compression. **Internat. J. Pharmaceut.**, v. 495, n. 1, p. 290–301, 2015.

Fang, F.; Li, Z.-S.; Cai, N.-S. Experiment and Modeling of CO2 Capture from Flue Gases at High Temperature in a Fluidized Bed Reactor with Ca-Based Sorbents. **Energy & Fuels**, v. 23, n. 1, p. 207–216, 2009.

Fang, W.; Jingdai, W.; Yongrong, Y. Distribution of Electrostatic Potential in a Gas-Solid Fluidized Bed and Measurement of Bed Level. **Industrial & Engineering Chemistry Research**, v. 47, n. 23, p. 9517–9526, dez. 2008.

Di Felice, R. The voidage function for fluid-particle interaction systems. **International Journal of Multiphase Flow**, v. 20, n. 1, p. 153–159, fev. 1994.

Feng, Y.; Yu, A. Microdynamic modelling and analysis of the mixing and segregation of binary mixtures of particles in gas fluidization. **Chemical Engineering Science**, v. 62, n. 1-2, p. 256–268, jan. 2007.

Feng, Y. Q.; Yu, A. B. Assessment of Model Formulations in the Discrete Particle Simulation of Gas-Solid Flow. **Industrial & Engineering Chemistry Research**, v. 43, n. 26, p. 8378–8390, dez. 2004.

Formisani, B.; Girimonte, R.; Longo, T. The fluidization process of binary mixtures of solids: Development of the approach based on the fluidization velocity interval. **Powder Technology**, v. 185, n. 2, p. 97–108, jul. 2008.

Fotovat, F.; Bi, X. T.; Grace, J. R. Electrostatics in gas-solid fluidized beds: A review. **Chemical Engineering Science**, v. 173, p. 303–334, dez. 2017.

Fung, K. Y.; Ng, K. M. Product-centered processing: Pharmaceutical tablets and capsules. **AIChE Journal**, v. 49, n. 5, p. 1193–1215, 2003.

Gao, W.; Farahani, M. R.; Jamil, M. K.; Siddiqui, M. K.; Siddiqui, H. M. A.; Imran, M.; Rezaee-Manesh, R. Kinetic modeling of pyrolysis of three Iranian waste oils in a micro-fluidized bed. **Petroleum Science and Technology**, v. 35, n. 2, p. 183–189, jan. 2017.

Geldart, D. Types of gas fluidization. **Powder Technol.**, v. 7, n. 5, p. 285–292, 1973.

Gibilaro, L.; Rowe, P. A model for a segregating gas fluidised bed. **Chemical Engineering Science**, v. 29, n. 6, p. 1403–1412, jun. 1974.

Gidaspow, D. Multiphase flow and fluidization : Continuum and kinetic theory descriptions. p. 467, 1994.

Glasser, B. J.; Kevrekidis, I. G.; Sundaresan, S. Fully developed travelling wave solutions and bubble formation in fluidized beds. **Journal of Fluid Mechanics**, v. 334, p. 157–188, mar. 1997.

Gomez, M.; McCollum, J.; Wang, H.; Bachchhav, S.; Tetreau, I.; Gerhardt, A.; Press, C.; Kramer, R. M.; Fox, C. B.; Vehring, R. Evaluation of the stability of a spray-dried tuberculosis vaccine candidate designed for dry powder respiratory delivery. **Vaccine**, v. 39, n. 35, p. 5025–5036, 2021.

Goniva, C.; Kloss, C.; Deen, N. G.; Kuipers, J. A.; Pirker, S. Influence of rolling friction on single spout fluidized bed simulation. **Particuology**, v. 10, n. 5, p. 582–591, out. 2012.

Guo, F.; Dong, Y.; Fan, P.; Lv, Z.; Yang, S.; Dong, L. Catalytic decomposition of biomass tar compound by calcined coal gangue: A kinetic study. **Int. J. Hydrogen Energ.**, v. 41, n. 31, p. 13380–13389, 2016.

Guo, Q. J.; Xu, Y.; Yue, X. Fluidization characteristics in micro-fluidized beds of various inner diameters. **Chemical Engineering and Technology**, v. 32, n. 12, p. 1992–1999, 2009.

Heida, R.; Hinrichs, W. L.; Frijlink, H. W. Inhaled vaccine delivery in the combat against respiratory viruses: A 2021 overview of recent developments and implications for COVID-19. **Expert Rev. Vaccines**, v. 21, n. 7, p. 957–974, 2022.

Hernández-Jiménez, F.; Sánchez-Prieto, J.; Cano-Pleite, E.; Soria-Verdugo, A. Lateral solids meso-mixing in pseudo-2D fluidized beds by means of TFM simulations. **Powder Technology**, v. 334, p. 183–191, jul. 2018.

Hernández-Neuta, I.; Pereiro, I.; Ahlford, A.; Ferraro, D.; Zhang, Q.; Viovy, J.-L.; Descroix, S.; Nilsson, M. Microfluidic magnetic fluidized bed for DNA analysis in continuous flow mode. **Biosensors and Bioelectronics**, v. 102, p. 531–539, abr. 2018.

Hoef, M. A. V. D.; Beetstra, R.; Kuipers, J. A. M. Lattice-Boltzmann simulations of low-Reynolds-number flow past mono- and bidisperse arrays of spheres: Results for the permeability and drag force. **Journal of Fluid Mechanics**, v. 528, p. 233–254, abr. 2005.

Homsy, G. M.; El-Kaissy, M. M.; Didwinia, A. Instability waves and the origin of bubbles in fluidized beds—II Comparison with theory. **International Journal of Multiphase Flow**, v. 6, n. 4, p. 305–318, ago. 1980.

Huang, J.; Garmise, R. J.; Crowder, T. M.; Mar, K.; Hwang, C. R.; Hickey, A. J.; Mikszta, J. A.; Sullivan, V. J. A novel dry powder influenza vaccine and intranasal delivery technology: Induction of systemic and mucosal immune responses in rats. **Vaccine**, v. 23, n. 6, p. 794–801, 2004.

Hudson, C.; Briens, C. L.; Prakash, A. Effect of inclination on liquid-solid fluidized beds. **Powder Technology**, v. 89, n. 2, p. 101–113, nov. 1996.

Jackson, R. The mechanics of fluidized beds: I. The stability of the state of uniform fluidization. **TRANS. INSTN CHEM. ENGERS**, v. 41, p. 13, 1963.

Jazayeri, B. Applications for Chemical Production and Processing. In: **Handbook of Fluidization and Fluid-Particles Systems**. New York: Marcel Dekker, 2003, (Chemical Industries, 91). p. 421–444. ISBN 978-0-8247-0259-5.

Jia, L.; Dufour, A.; Le Brech, Y.; Authier, O.; Mauviel, G. On-line analysis of primary tars from biomass pyrolysis by single photoionization mass spectrometry: Experiments and detailed modelling. **Chemical Engineering Journal**, v. 313, p. 270–282, abr. 2017.

Jiang, G.; Joshi, S. B.; Peek, L. J.; Brandau, D. T.; Huang, J.; Ferriter, M. S.; Woodley, W. D.; Ford, B. M.; Mar, K. D.; Mikszta, J. A.; Hwang, C. R.; Ulrich, R.; Harvey, N. G.; Middaugh, C. R.; Sullivan, V. J. Anthrax vaccine powder formulations for nasal mucosal delivery. **J. Pharm. Sci.**, v. 95, n. 1, p. 80–96, 2006.

Jiang, Z.; Hagemeier, T.; Bück, A.; Tsotsas, E. Color-PTV measurement and CFD-DEM simulation of the dynamics of poly-disperse particle systems in a pseudo-2D fluidized bed. **Chemical Engineering Science**, v. 179, p. 115–132, abr. 2018.

Johnson, K. L. **Contact Mechanics**. 1. ed. [S.l.]: Cambridge University Press, 1985. ISBN 978-0-521-25576-9 978-0-521-34796-9 978-1-139-17173-1.

Jung, J.; Gidaspow, D.; Gamwo, I. K. Measurement of two kinds of granular temperatures, stresses, and dispersion in bubbling beds. **Industrial and Engineering Chemistry Research**, v. 44, n. 5, p. 1329–1341, mar. 2005.

Katstra, W. E.; Palazzolo, R. D.; Rowe, C. W.; Giritlioglu, B.; Teung, P.; Cima, M. J. Oral dosage forms fabricated by Three Dimensional Printing™. **J. Control. Release**, v. 66, n. 1, p. 1–9, 2000.

Kloss, C.; Goniva, C.; Hager, A.; Amberger, S.; Pirker, S. Models, algorithms and validation for opensource DEM and CFD-DEM. **Progress in Computational Fluid Dynamics**, v. 12, n. 2-3, p. 140–152, 2012.

Kornblum, S. S.; Hirschorn, J. O. Dissolution of Poorly Water-Soluble Drugs I: Some Physical Parameters Related to Method of Micronization and Tablet Manufacture of a Quinazolinone Compound. **J. Pharm. Sci.**, v. 59, n. 5, p. 606–609, 1970.

Kunii, D.; Levenspiel, O. **Fluidization Engineering**. 2nd. ed. Boston: Butterworth-Heinemann, 1991. ISBN 0-409-90233-0.

Kuyukina, M. S.; Ivshina, I. B.; Serebrennikova, M. K.; Krivorutchko, A. B.; Podorozhko, E. A.; Ivanov, R. V.; Lozinsky, V. I. Petroleum-contaminated water treatment in a fluidized-bed bioreactor with immobilized Rhodococcus cells. **International Biodeterioration & Biodegradation**, v. 63, n. 4, p. 427–432, jun. 2009.

Kwak, W.; Rout, P. R.; Lee, E.; Bae, J. Influence of hydraulic retention time and temperature on the performance of an anaerobic ammonium oxidation fluidized bed membrane bioreactor for low-strength ammonia wastewater treatment. **Chemical Engineering Journal**, v. 386, p. 123992, abr. 2020.

Lacey, P. M. C. Developments in the theory of particle mixing. **Journal of Applied Chemistry**, v. 4, n. 5, p. 257–268, maio 1954.

Li, S.; Zhao, P.; Xu, J.; Zhang, L.; Wang, J. Direct comparison of CFD-DEM simulation and experimental measurement of Geldart A particles in a micro-fluidized bed. **Chemical Engineering Science**, v. 242, p. 116725, out. 2021.

Li, T.; Zhang, H.; Liu, M.; Huang, Z.; Bo, H.; Dong, Y. DEM study of granular discharge rate through a vertical pipe with a bend outlet in small absorber sphere system. **Nucl. Eng. Des.**, v. 314, p. 1–10, 2017.

Li, X.; Li, Q.; Wang, L.; Jia, L.; Sun, Z.; Wang, X. Influence of oblique angle on hydrodynamics of gas-solid fluidization in micro fluidized bed. In: **2017 Chinese Automation Congress (CAC)**. [S.l.: s.n.], 2017. p. 5709–5714.

Li, Y.; Xu, Y.; Thornton, C. A comparison of discrete element simulations and experiments for 'sandpiles' composed of spherical particles. **Powder Technology**, v. 160, n. 3, p. 219–228, dez. 2005.

Liu, D.; Chen, X. Lateral solids dispersion coefficient in large-scale fluidized beds. **Combustion and Flame**, v. 157, n. 11, p. 2116–2124, nov. 2010.

Liu, D.; Kwauk, M.; Li, H. Aggregative and particulate fluidization—The two extremes of a continuous spectrum. **Chemical Engineering Science**, v. 51, n. 17, p. 4045–4063, set. 1996.

Liu, D.; Song, J.; Ma, J.; Chen, X.; van Wachem, B. Gas flow distribution and solid dynamics in a thin rectangular pressurized fluidized bed using CFD-DEM simulation. **Powder Technology**, v. 373, p. 369–383, ago. 2020.

Liu, D.; van Wachem, B. Comprehensive assessment of the accuracy of CFD-DEM simulations of bubbling fluidized beds. **Powder Technology**, v. 343, p. 145–158, fev. 2019.

Liu, J.; Ren, Y.; Yao, S. Repeated-batch Cultivation of Encapsulated Monascus purpureus by Polyelectrolyte Complex for Natural Pigment Production. **Chinese Journal of Chemical Engineering**, v. 18, n. 6, p. 1013–1017, dez. 2010.

Mao, Y.; Dong, L.; Dong, Y.; Liu, W.; Chang, J.; Yang, S.; Lv, Z.; Fan, P. Fast co-pyrolysis of biomass and lignite in a micro fluidized bed reactor analyzer. **Bioresource Technology**, v. 181, p. 155–162, abr. 2015.

Mindlin, R. D.; Deresiewicz, H. Elastic Spheres in Contact Under Varying Oblique Forces. **Journal of Applied Mechanics**, v. 20, n. 3, p. 327–344, set. 1953.

Müller, C. R.; Holland, D. J.; Sederman, A. J.; Scott, S. A.; Dennis, J. S.; Gladden, L. F. Granular temperature: Comparison of magnetic resonance measurements with discrete element model simulations. **Powder Technology**, v. 184, n. 2, p. 241–253, maio 2008.

Newby, R. A. Applications for Gasifiers and Combustors. In: **Handbook of Fluidization and Fluid-Particles Systems**. New York: Marcel Dekker, 2003, (Chemical Industries, 91). p. 397–420. ISBN 978-0-8247-0259-5.

Norouzi, H. R.; Zarghami, R.; Sotudeh-Gharebagh, R.; Mostoufi, N. **Coupled CFD-DEM Modeling**. Chichester, UK: John Wiley & Sons, Ltd, 2016. ISBN 978-1-119-00531-5.

O'Dea, D. P.; Rudolph, V.; Chong, Y. O.; Leung, L. S. The effect of inclination on fluidized beds. **Powder Technology**, v. 63, n. 2, p. 169–178, nov. 1990.

Oke, O.; Van Wachem, B.; Mazzei, L. Lateral solid mixing in gas-fluidized beds: CFD and DEM studies. **Chemical Engineering Research and Design**, v. 114, p. 148–161, out. 2016.

Oliveira, H. B.; Franklin, E. M. Dataset for 'Bidisperse micro fluidized beds: Effect of bed inclination on mixing'. **Mendeley Data**, 2023.

Oliveira, H. B.; Franklin, E. M. Bidisperse micro fluidized beds: Effect of bed inclination on mixing. **Physics of Fluids**, v. 36, n. 1, p. 013303, jan. 2024.

Oliveira, V. P. S.; Borges, D. S.; Franklin, E. M. Crystallization and refluidization in very-narrow fluidized beds. **Physics of Fluids**, v. 35, n. 9, p. 093306, set. 2023.

Pereiro, I.; Bendali, A.; Tabnaoui, S.; Alexandre, L.; Srbova, J.; Bilkova, Z.; Deegan, S.; Joshi, L.; Viovy, J.-L.; Malaquin, L.; Dupuy, B.; Descroix, S. A new microfluidic approach for the one-step capture, amplification and label-free quantification of bacteria from raw samples. **Chemical Science**, v. 8, n. 2, p. 1329–1336, 2017.

Del Pozo, M.; Briens, C. L.; Wild, G. Effect of column inclination on the performance of three-phase fluidized beds. **AIChE Journal**, v. 38, n. 8, p. 1206–1212, 1992.

Qie, Z.; Alhassawi, H.; Sun, F.; Gao, J.; Zhao, G.; Fan, X. Characteristics and applications of micro fluidized beds (MFBs). **Chemical Engineering Journal**, v. 428, p. 131330, jan. 2022.

Raganati, F.; Ammendola, P.; Chirone, R. CO2 capture performances of fine solid sorbents in a sound-assisted fluidized bed. **Powder Technology**, v. 268, p. 347–356, dez. 2014.

Raganati, F.; Gargiulo, V.; Ammendola, P.; Alfe, M.; Chirone, R. CO2 capture performance of HKUST-1 in a sound assisted fluidized bed. **Chemical Engineering Journal**, v. 239, p. 75–86, mar. 2014.

Di Renzo, A.; Rito, G.; Di Maio, F. P. Systematic Experimental Investigation of Segregation Direction and Layer Inversion in Binary Liquid-Fluidized Bed. **Processes**, v. 8, n. 2, p. 177, fev. 2020.

Richardson, J.; Zaki, W. Sedimentation and fluidisation: Part I. **Chemical Engineering Research and Design**, v. 32, p. S82–S100, 1954.

Rodríguez-Rojo, S.; Marienfeld, J.; Cocero, M. RESS process in coating applications in a high pressure fluidized bed environment: Bottom and top spray experiments. **Chemical Engineering Journal**, v. 144, n. 3, p. 531–539, nov. 2008.

Rowe, P. A convenient empirical equation for estimation of the Richardson-Zaki exponent. **Chemical Engineering Science**, v. 42, n. 11, p. 2795–2796, 1987.

Schreiber, R.; Vogt, C.; Werther, J.; Brunner, G. Fluidized bed coating at supercritical fluid conditions. **The Journal of Supercritical Fluids**, v. 24, n. 2, p. 137–151, nov. 2002.

Shen, T.; Zhu, X.; Yan, J.; Shen, L. Design of micro interconnected fluidized bed for oxygen carrier evaluation. **Int. J. Greenh. Gas Con.**, v. 90, p. 102806, 2019.

Shi, K.; Tan, D. K.; Nokhodchi, A.; Maniruzzaman, M. Drop-On-Powder 3D Printing of Tablets with an Anti-Cancer Drug, 5-Fluorouracil. **Pharmaceutics**, v. 11, n. 4, p. 150, 2019.

Da Silva, C. A. M.; Butzge, J. J.; Nitz, M.; Taranto, O. P. Monitoring and control of coating and granulation processes in fluidized beds – A review. **Advanced Powder Technology**, v. 25, n. 1, p. 195–210, jan. 2014.

Stukowski, A. Visualization and analysis of atomistic simulation data with OVITO–the Open Visualization Tool. **Modelling and Simulation in Materials Science and Engineering**, v. 18, n. 1, p. 015012, jan. 2010.

Suryawanshi, P. L.; Gumfekar, S. P.; Bhanvase, B. A.; Sonawane, S. H.; Pimplapure, M. S. A review on microreactors: Reactor fabrication, design, and cutting-edge applications. **Chemical Engineering Science**, v. 189, p. 431–448, nov. 2018.

Tartan, M.; Gidaspow, D. Measurement of granular temperature and stresses in risers. **AIChE Journal**, v. 50, n. 8, p. 1760–1775, ago. 2004.

Tsuji, Y.; Kawaguchi, T.; Tanaka, T. Discrete particle simulation of two-dimensional fluidized bed. **Powder Technology**, v. 77, n. 1, p. 79–87, out. 1993.

Valverde, J. M.; Castellanos, A.; Quintanilla, M. A. S.; Gilabert, F. A. Effect of inclination on gas-fluidized beds of fine cohesive powders. **Powder Technology**, v. 182, n. 3, p. 398–405, mar. 2008.

Weller, H. G.; Tabor, G.; Jasak, H.; Fureby, C. A tensorial approach to computational continuum mechanics using object-oriented techniques. **Computers in Physics**, v. 12, n. 6, p. 620–631, nov. 1998.

Wen, C. Y.; Yu, Y. H. A generalized method for predicting the minimum fluidization velocity. **AIChE Journal**, v. 12, n. 3, p. 610–612, maio 1966.

Wu, G.; Yu, B.; Guan, Y.; Wu, X.; Zhang, K.; Li, Y. Mixing Characteristics of Binary Mixture with Biomass in a Gas-Solid Rectangular Fluidized Bed. **Energies**, v. 12, n. 10, p. 2011, maio 2019.

Wu, K.-J.; Chang, C.-F.; Chang, J.-S. Simultaneous production of biohydrogen and bioethanol with fluidized-bed and packed-bed bioreactors containing immobilized anaerobic sludge. **Process Biochemistry**, v. 42, n. 7, p. 1165–1171, jul. 2007.

Yi, Z.; Ullah, N.; Law, R.; Reay, D.; Vladimir Zivkovic. Investigation into the hydrodynamics of liquid-solid inclined micro-fluidized beds. **Resources Chemicals and Materials**, v. 1, p. 8–15, 2022.

Yu, J.; Yao, C.; Zeng, X.; Geng, S.; Dong, L.; Wang, Y.; Gao, S.; Xu, G. Biomass pyrolysis in a micro-fluidized bed reactor: Characterization and kinetics. **Chem. Eng. J.**, v. 168, n. 2, p. 839–847, 2011.

Zeng, X.; Wang, F.; Wang, Y.; Li, A.; Yu, J.; Xu, G. Characterization of Char Gasification in a Micro Fluidized Bed Reaction Analyzer. **Energy & Fuels**, v. 28, n. 3, p. 1838–1845, mar. 2014.

Zhang, Y.; Goh, K.-L.; Ng, Y. L.; Chow, Y.; Wang, S.; Zivkovic, V. Process intensification in micro-fluidized bed systems: A review. **Chemical Engineering and Processing - Process Intensification**, v. 164, p. 108397, jul. 2021.

Zhang, Y.; Jin, B.; Zhong, W. Experiment on particle mixing in flat-bottom spout–fluid bed. **Chemical Engineering and Processing: Process Intensification**, v. 48, n. 1, p. 126–134, jan. 2009.

Zhang, Y.; Yao, M.; Gao, S.; Sun, G.; Xu, G. Reactivity and kinetics for steam gasification of petroleum coke blended with black liquor in a micro fluidized bed. **Applied Energy**, v. 160, p. 820–828, dez. 2015.